

RESEARCH ARTICLE

Identifying climate models based on their daily output using machine learning

Lukas Brunner¹ * and Sebastian Sippel² 

¹Department of Meteorology and Geophysics, University of Vienna, Vienna, Austria

²Institute for Atmospheric and Climate Science, ETH Zurich, Zurich, Switzerland

*Corresponding author. Email: l.brunner@univie.ac.at

Received xx xxx xxxx

Keywords: climate model evaluation; reanalysis; machine learning; logistic regression; convolutional neural networks

NOTE: This manuscript has been submitted to Environmental Data Science and has not yet undergone peer-review.

Abstract

Climate models are primary tools for investigating processes in the climate system, projecting future changes, and informing decision makers. The latest generation of models provides increasingly complex and realistic representations of the real climate system, while there is also growing awareness that not all models produce equally plausible or independent simulations. Therefore, many recent studies have investigated how models differ from observed climate and how model dependence affects model output similarity, typically drawing on climatological averages over several decades. Here, we show that temperature maps of individual days drawn from datasets never used in training can be robustly identified as “model” or “observation” using the CMIP6 model archive and four observational products. An important exception is a prototype storm-resolving simulation from ICON which cannot be unambiguously assigned to either category. These results highlight that persistent differences between simulated and observed climate emerge at short time scales already, but very high-resolution modelling efforts may be able to overcome some of these shortcomings. Moreover, individual datasets can also be identified, with up to 83 % days correctly classified into one of 47 categories. Misclassifications occur mostly between models developed at the same institution, suggesting that effects of shared code, previously documented only for climatological timescales, already emerge at the level of individual days. Our results thus demonstrate that the use of machine learning classifiers, once trained, can overcome the need for several decades of data to evaluate a given model. This opens up new avenues to test model performance and independence on much shorter timescales.

Impact Statement

Climate models are used to study changes in the climate system and to inform decision makers. While models are getting better and better at representing the observed climate, some differences compared to observations remain. To isolate them from the influence of weather, such differences are typically investigated in climatological averages over several decades. Here, we show that maps from individual days are sufficient to robustly identify models using statistical and machine learning classifiers that have first been trained on different models and/or in a different time period. These results provide new ways of evaluating and interpreting model-observation and model-model differences, on short time scales.

1. Introduction

Multi-model ensembles, such as the latest sixth Coupled Model Intercomparison Project (CMIP6; Eyring et al. [2016]), are widely used to investigate physical climate mechanisms, to attribute past and project future changes, and inform political decisions. However, there is a growing awareness in the climate community that not all models included in CMIP provide equally plausible and independent simulations of the climate system [Tebaldi and Knutti, 2007, Knutti, 2010, Bishop and Abramowitz, 2013, Annan and Hargreaves, 2017, Eyring et al., 2019]. Model evaluation methods, typically based on multi-decadal climatological averages to minimise the effect of internal variability on short timescales, have identified persistent biases across models compared to observations and highlighted the impact of model dependence on the similarity of model outputs [Masson and Knutti, 2011, Knutti et al., 2013, Boé, 2018, Brunner et al., 2020, Bock et al., 2020]. Both, model bias and model dependence, are ultimately due to the parameterizations used to represent processes that cannot be explicitly resolved in simulations of the observed climate in numerical models.

Work is ongoing to further reduce these parametrizations in new generations of kilometre-scale, storm-resolving global models with the ultimate aim of creating a digital twin of Earth [Bauer et al., 2021, Rackow et al., 2021, Hohenegger et al., 2022]. These developments continue to blur the boundaries between weather prediction, climate prediction, and climate projection [Meehl et al., 2021] and call for new, innovative evaluation methods that allow models to be compared with observations and with each other on weather timescales. For example, biases in climate models can emerge over relatively short timescales when a model is initialised with an observed state, and pinpointing these biases may help model development [Palmer, 2016]. This includes investigating the extent to which model biases and dependencies can be identified on such short timescales and how this can be interpreted.

A range of recent studies have demonstrated the potential of statistical and machine learning in climate science. These include approaches for seasonal prediction [Gibson et al., 2021], to identify forced signals from spatial patterns of temperature, precipitation, and humidity [Barnes et al., 2019, Sippel et al., 2020, De Vries et al., 2022], to explore the role of single forcing agents [Labe and Barnes, 2021], to predict modes of atmosphere-ocean variability [Gordon et al., 2021], and, most recently, to contrast models and observations [Labe and Barnes, 2022]. Here, we investigate the potential of such statistical and machine learning classifiers to separate models from observations and from each other on the basis of daily data, and thus in the presence of considerable noise arising from the internal variability on weather timescales. We argue that the typically applied temporal aggregation over several years or even decades can be overcome and that future model evaluation methods might be able to be based on considerably shorter time periods, at least once classifiers have been trained. This can allow the investigation of new or updated models for which decades of data are not yet available, as showcased by the inclusion of one year of experimental storm-resolving simulations provided by the NextGEMS project¹.

The work is guided by two main questions which are detailed and discussed in sections 3 and 4: based on daily temperature output (1) can out-of-sample test datasets (i.e., datasets never used in training) of models and observations reliably be identified as different from each other and (2) can temporally out-of-sample test data be identified by their name, even if they come from a different climate regime? The datasets and methods are presented in section 2 and the results are summarised and interpreted in section 5.

¹<https://nextgems-h2020.eu>

2. Data and methods

2.1. Model and observational data

We use all available CMIP6 models which provide daily data for 2 m surface air temperature in the historical period. In total, this amounts to 43 models, which can be broadly grouped into 22 families by developing institutions (see table S3 in the supplement for a full list). To represent the observations we use four datasets selected to cover some of the diversity in observational products: (1) the fifth generation of the European Centre for Medium-Range Weather Forecasts (ECMWF) Retrospective Analysis (ERA5; Hersbach et al. [2020]); (2) the Modern-Era Retrospective analysis for Research and Applications version 2 (MERRA2; Gelaro et al. [2017], GMAO [2015]); (3) the Twentieth Century Reanalysis version 3 (20CR; Slivinski et al. [2021]), which assimilates only surface pressure observations and, hence, relies considerably more on modelling for its output; (4) the Daily Optimum Interpolation Sea Surface Temperature dataset version 2 (DOISST; Huang et al. [2021]), which could be considered as more direct observations compared to the other datasets. The first three observational datasets provide 2 m surface air temperature also over the oceans equivalent to the models, while DOISST is based on interpolated in situ and remote sensing measurements of sea surface temperature, which is a slightly different but closely related measure of temperature.

The time period from 1982 to 2014 is used to match the first availability of all observational datasets and the end of the historical forcing period in CMIP6, respectively and all daily temperature fields (including the high-resolution simulations) are regridded to $2.5^\circ \times 2.5^\circ$ resulting in a total of $10'368$ grid cells (72 latitudes \times 144 longitudes). Since DOISST does not provide data on land we apply a common land-sea mask to all datasets, using only the $6'888$ ocean grid cells. Sensitivity analysis (omitting DOISST) shows that results are similar if the analysis is based on all grid cells.

In addition, we use temperature projections for the end of the century (2091-2100) driven by the high emission scenario SSP5-8.5 [Meinshausen et al., 2020], where available, to test the robustness of our approach under severe warming (see table S3). Finally, we also draw on one year (February 2020 to January 2021) of prototype data from cycle one of the NextGEMS project and use global temperature fields from an ICON run with an atmospheric resolution of 5 km (experiment ID: dpp066; Hohenegger et al. [2022]).

2.2. Statistical and machine learning classifiers

We use two different statistical and machine learning methods to separate models from observations, and from each other. First, logistic regression, which allows insights into the learned coefficients but has the limitation of being a linear method. Second, a convolutional neural network (CNN) which represents rather the other end of the complexity spectrum, being able to learn non-linear spatial relations between features but lacking the easy interpretability of logistic regression.

Logistic regression is linear in its parameters and takes an $M \times N$ matrix as input, where N is the number of samples (days) and M is the number of features (ocean grid cells). For training an additional vector of length N is provided containing the true labels y_n (i.e., 0 for “model” and 1 for “observation”) for each sample. A continuous predicted probability \hat{p}_n is then assigned to each sample X_n based on its features $x_{n,m}$ and the regression parameters w_m via the logistic function:

$$\hat{p}_n = \frac{1}{1 + \exp\left(-\left(w_0 + \sum_{m=1}^M w_m x_{n,m}\right)\right)}$$

The outcome is in $[0, 1]$ with 1 indicating the highest chance that a given day belongs into the “observation” category and at the same time the lowest chance that it belongs into the “model” category since the categories are complementary:

$$\hat{p}(y_n = 0|X_n) = 1 - \hat{p}(y_n = 1|X_n)$$

The predicted category \hat{y}_n is based on this probability \hat{p}_n with a decision threshold of 0.5. The logistic regression classifier is constrained by a L_2 regularisation (i.e., a penalty on the squared sum of regression coefficients w_m) to avoid overfitting and to ensure smooth coefficients in space. Overall coefficients w_m are searched to minimise the expression:

$$\min_w \left\{ -C \sum_{n=1}^N [y_n \log(\hat{p}_n) + (1 - y_n) \log(1 - \hat{p}_n)] + \sum_{m=0}^M w_m^2 \right\}$$

Note that in the implementation based on scikit-learn² used in this manuscript the regularisation parameter C is multiplied with the residuals rather than with the coefficients, meaning that smaller values of C lead to stronger regularisation. C is optimised using 5-fold cross-validation. More general details on regularised logistic regression can be found, for instance, in [Hastie et al. \[2009\]](#).

To complement the logistic regression classifier we use a CNN as a second method. Deep neural networks, such as CNNs, can have considerably more trainable parameters (often organised in multiple layers) and can be less interpretable than traditional methods. This means that they can be, on the one hand, more prone to overfitting, but, on the other hand, can also learn more complex, non-linear relationships in the data. Therefore, their use in different scientific disciplines, not least in climate sciences, has been rapidly increasing in recent years [[Kashinath et al., 2021](#), [Hsieh, 2022](#)]. Due to their complexity many different design choices in the exact layout of the network are possible, here we use an out-of-the-box setup for image classification without hyper-parameter tuning but adjusted to the resolution of the daily temperature maps used in the input layer. Overall, the CNN consists of an input layer, eight hidden layers, and an output layer. See table S2 in the supplement for details about the layout.

The 2-dimensional temperature fields from each day can directly be interpreted by the CNN equivalent to a image classification task, therefore, the input layer takes a $K \times L \times N \times 1$ matrix where N is, again, the number of days, K the number of latitudes, L the number of longitudes, and 1 a single colour channel representing the temperature values. Note that for this case land grid cells are included but set to a constant fill value. The convolutional layers use the rectified linear unit as activation function, while the output layer uses the softmax operator to assign probabilities to each of classification categories z_n :

$$\hat{p}_n = \frac{e^{z_n}}{\sum_n e^{z_n}}$$

This means that, in contrast to the logistic regression, the CNN is set up to separate also between multiple output categories (multi-class case) and a given input is identified as belonging to the class with the highest probability. For the binary case with only the “model” and “observation” classes, discussed in the first part of the manuscript, this means that the probabilities are complementary and the threshold for assignment is 0.5 as for the logistic regression. To avoid overfitting for the CNN, part of the training data are used for validation during the training process and an early stopping criterion is applied on the validation loss. The evolution of loss and accuracy during the training epochs are shown in figures S2 and S3 in the supplement. All classifiers are mostly well-calibrated with the CNN showing a tendency for overconfidence, in particular, for the multi-class cases (figures S4 to S6).

²<https://scikit-learn.org>

The performance of the classifiers is, on the one hand, assessed using the overall accuracy which is defined as the number of correct predictions divided by the number of total predictions. On the other hand, also the confidence in the predictions is assessed based on the probabilities assigned to each test sample from each dataset individually.

2.3. Out-of-sample frameworks and pre-processing

We use daily, land-masked temperature fields as samples, resulting in 6'888 grid cells being used as features for the classification. The 2-dimensional daily fields are either used directly in the case of the CNN classifier or reduced to a 1-dimensional feature array in the case of logistic regression. Note that the changing grid cell area with latitude due to longitude convergence is not explicitly accounted for in this study but may be implicitly learned by the classifiers.

Training and validation days are drawn from the 20-year period 1982-2001. As test data all days from the two *temporally out-of-sample* 10-year periods 2005-2014 and 2091-2100 are used. Therefore all results are based on test samples that were never seen in training.

For the separation of “model” versus “observation” in section 3, we use an additional *dataset out-of-sample* framework to explore whether the learned parameters can be generalised to unseen datasets: a separate classifier is trained for each dataset, where all samples from the dataset in question are withheld from training. To be even stricter, for climate models not only the model in question is withheld in training, but also all closely related models (see table S3 in the supplement for a list of the model groups). We chose this approach because it has been shown that closely related models (i.e., models developed at the same institution) can have very similar output [Brunner et al., 2020]. The only exceptions to this are the regression coefficients shown in figure 1 and the bootstrap tests for which all datasets were used in training.

In both machine learning and climate modelling, there are different pre-processing and bias correction options and corresponding terminologies. These include more general approaches such as feature normalisation and more domain specific approaches such as bias correction. The latter are based on physical system understanding, such as the insight that the mean temperature bias is not a relevant predictor of a model's ability to simulate changes in the climate system [Giorgi and Coppola, 2010]. Here we opt for two domain specific bias-correction approaches from climate sciences: (1) from each daily temperature field, the mean over that field is removed and (2) from each daily temperature field, the seasonal mean temperature field is removed in addition to (1).

For (2) the seasonal mean temperature field is calculated individually for each dataset and only based on the training data. For each day-of-the-year and grid cell it is calculated as the average over ± 15 days around that day-of-the-year and over all training years (i.e., a mean over 31 days \times 20 years = 620 values). For the ICON model the seasonal cycle is estimated based on only one year (i.e., 31 values centred around each day of the year).

Finally, each sample is associated with one of two label types to be predicted by the machine learning classifiers: either “model”/“observation” (binary case) or the name of the dataset (multi-class case; see the dataset ID column in table S3). A summary of all classifiers, bias corrections, and out-of-sample strategies employed in this work can be found in table S1 in the supplement. Figures S7 and S8 show an example test day from each of the datasets and for the two pre-processing cases, respectively. While, in the first case, latitudinal temperature gradients due to differing solar insolation clearly dominate the temperature pattern, in the second case patches of regionally cooler or warmer temperatures emerge, related to the synoptic atmospheric conditions on that day. Note that models are not expected to simulate the same weather on any respective day in contrast to the observations. This is due to the fact that the four observation-based datasets assimilate measurements from the same day leading to very similar surface temperature patterns. The models, in turn, are free-running and therefore simulate different synoptic situations and related temperature patterns.

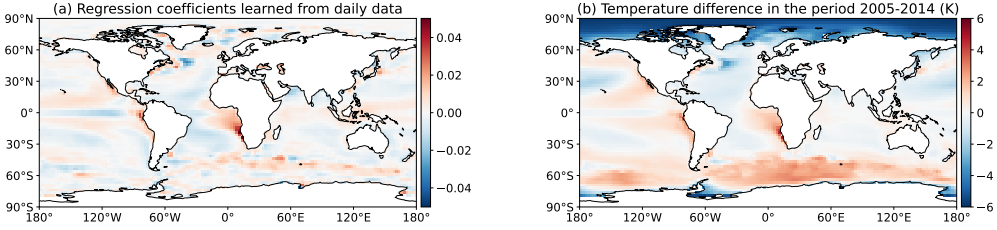


Figure 1. (a) Logistic regression coefficients learned from 17'200 randomly drawn daily samples in the period 1982-2001 to separate models and observations. (b) Climatological mean, multi-model mean temperature difference to the mean over the four observational datasets in the period 2005-2014. See figure S7 for corresponding maps of the individual models. Coefficients and climatologies are calculated from daily data with the global mean removed.

3. Separating models and observations

3.1. Regression coefficient maps to separate models and observations

First, we train a single logistic regression classifier on all available datasets to establish the regularisation parameter and examine the learned coefficients. For this case we use data with only the global mean removed. We use 200 different, randomly drawn training days from each of the 43 models resulting in 8'600 training samples labelled “model” which are matched by 8'600 random days labelled “observation” (2'150 from each of the four observational datasets). The classifier manages to correctly identify the vast majority of test samples for this setup so that the number of training samples was limited to this amount to save computational resources. It can be assumed that increasing the number of training samples would slowly improve the classification skill even further. The results are also robust to using different random training samples (see section S3 in the supplement for results from a 100-member bootstrap test).

Since temperatures between neighbouring grid cells, used as features, are not independent, the 5-fold cross-validation yields a strong L_2 regularisation parameter of about $C = 0.002$, which is used for all logistic regression classifiers in this section. The spatial patterns in the features that are important for separating models and observations are reflected in the regression coefficients learned by the classifier and are shown in figure 1a. The distribution of the coefficients identifies areas important for the separation of climate models and observations on a daily scale. In addition, the sign of the coefficients can be interpreted physically, with positive values indicating regions where models tend to be warmer than the observations and vice-versa.

The most prominent region of negative coefficients is found in the North Atlantic, near the so-called North Atlantic warming hole [Chemke et al., 2020, Keil et al., 2020]. Here models appear to systematically underestimate temperatures on a daily basis compared with observations and relative to the global mean. In contrast, there are regions of high coefficients at the eastern edges of the Pacific and Atlantic ocean basins. These regions correspond to persistent model biases in the representation of clouds and their radiative effects which are known to occur on all timescales from daily to decadal [Williams et al., 2013, Ma et al., 2014, Brient et al., 2019, Bock et al., 2020, Chen et al., 2022]. In the equatorial Pacific, known as a region with notorious climate model biases that typically show too cold and too narrow equatorial cold tongues, negative coefficients are also found by the logistic regression classifier. This is accompanied by warm biases to the north and south (shown as positive regression coefficients) associated with the models' representation of the intertropical convergence zone [Hirota et al., 2011, Li and Xie, 2014, Tian and Dong, 2020]. Overall, there are notable consistencies in several of the large scale patterns between the logistic regression coefficients and the climatological mean, multi-model mean biases (figures 1a and b).

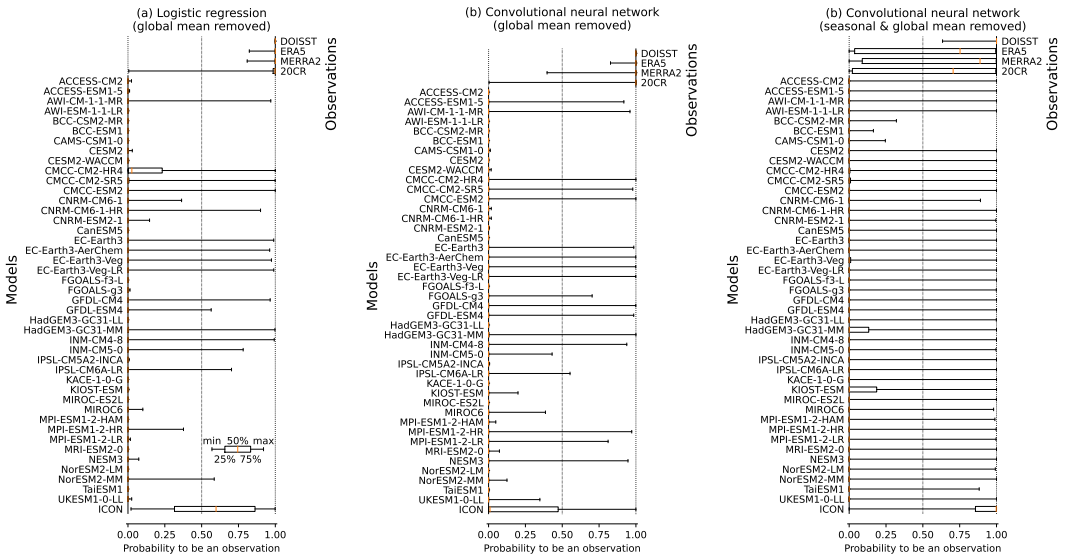


Figure 2. Distribution of predicted probabilities for the dataset out-of-sample test days: for each dataset the probabilities are estimated by a classifier which has not been trained on this dataset. The vertical dotted line at 0.5 marks the decision threshold between the two categories. The ICON model is never used in training and has only one year of data available. (a) Results for logistic regression classifiers using data with the daily global mean removed. (b) Same as (a) but for the convolutional neural network. (c) Same as (b) but using data with the seasonal cycle removed in addition.

However, there are also several regions where the two do not match, such as high northern latitudes, parts of the southern ocean, and the Antarctic coast. This can be an indication that the corresponding features are not shared across all (or at least most) potential days drawn from different models and from across the seasonal cycle. The high northern latitudes are briefly discussed here as one example for such a case with the clear climatological cold bias in the multi-model mean (figure 1b) not being reflected in corresponding patterns in the regression coefficients (figure 1a). This is probably caused by a combination of reasons as this region is known for its large (climatological) model spread (see, for example [Notz and Community \[2020\]](#) and figure S9), its seasonally varying biases with cold biases mainly coming from the winter season [[Davy and Outten, 2020](#)], and large internal variability which reduces the size of the regression coefficients there [[Barnes et al., 2019](#), [Sippel et al., 2020](#)]. In general, it is, therefore, not a priori clear if patterns important for the classification of individual days and long-term climatological biases (averaged over multiple models) would match at all, but our findings show that for several regions this is the case.

3.2. Logistic regression classification of out-of-sample datasets

In the rest of this section we use the *dataset out-of-sample* approach described in section 2.3 to show whether the classifiers can be generalised to datasets unseen in training. The probabilities assigned to the test samples by each corresponding classifier are aggregated in figure 2a. For the vast majority of cases the logistic regression classifiers assign the correct category with close to 100 % probability leading to an overall accuracy of 99.4 % (excluding the ICON model discussed below). Some of this skill may be due to remaining dependencies across families, which were quite loosely defined based on institutions in this study. However, it could also be an indication for the existence of persistent distinguishing features that can be transferred between models even in presence of the large internal variability on daily timescales.

For several models a fraction of test samples is predicted with less certainty (boxes and whiskers emerging from the zero-line in figure 2a and reliability diagram in figure S4). The model families most prone to get confused with observations are CMCC, CNRM, EC-Earth3, GFDL, and INM. An intuitive interpretation of this behaviour might be that these models provide the “best” representation of “true” temperatures on a daily basis as they are most similar to the observations (at least viewed through the lens of logistic regression). However, this is not conclusive and would require additional evidence. First, there are only very few samples with a non-zero probability of belonging into the observation category for any given model, so the confusion could be due to chance (i.e., a model sample could be classified as observations, but for the wrong reasons so that no conclusion should be drawn about the overall performance of the model). A second important consideration is possible codebase overlap also between models and the observational datasets, which could be picked up by the classifier as discussed in more detail in section 4 below. Nevertheless, the approach of intentionally exploiting misclassifications of models as observations is still a promising avenue for future research as recently also highlighted by work from [Labe and Barnes \[2022\]](#), who find that for the Arctic test samples from observations are most prone to get confused for certain models.

Focusing on model families that provide high and low resolution variants of the same model (AWI, CMCC, CNRM, HadGEM, MPI, and NorESM2), one can speculate about some resolution dependence in the probability to be misclassified. Several finer-resolution model variants appear to have a higher chance to be misclassified compared to their coarser-resolution siblings (model names including HR, MR/MM, or LR/LL indicating relatively higher to lower resolution in figure 2a). Such a behaviour would be consistent with studies based on climatological timescales such as the findings of [Bock et al. \[2020\]](#) who note that long-standing regional model biases are smaller in higher resolution versions of the same model.

3.3. *Classifying samples from the kilometre-scale ICON model*

To investigate this further and to highlight a potential application of our approach, we include preliminary results from the NextGEMS project and predict samples from one year of data from a global, storm-resolving (atmospheric resolution 5 km) simulation using ICON [[Hohenegger et al., 2022](#)]. Due to the high resolution, processes that need to be parameterised in CMIP6-type models, can be explicitly resolved in ICON, which can be expected to have considerable impacts also on the daily temperature fields. However, they do not obviously show in the climatological mean difference to the observations which is comparable to coarser resolved models and shows similar patterns, although we note that this could be a coincidence given that only a single year is used (see figure S10 in the supplement). This means that based on the comparison of climatologies alone, one might assume that the logistic regression classifier should be able to unambiguously identify ICON as a model.

To investigate this, we classify test samples from ICON using the logistic regression classifier trained on all other datasets. However, despite the similar climatologies, the classifier is unable to clearly identify ICON as either model or observation with about half of the samples predicted to be in either category. This indicates that the classification is (at least partly) based on more complex relationships in the high-dimensional feature space than can be easily assessed by the comparison shown in figure 1. The explicit resolution of processes which are parameterised in coarser models seems to lead to differences in the daily temperature fields in ICON that prevent a correct classification, even though they do not clearly emerge in the climatological mean. This points to a potentially highly encouraging emergent behaviour of the ICON simulations, but in principle some effect of compensating errors cannot be excluded, and hence we warrant a careful interpretation of this result, which will be verified as soon as a longer simulation with this model is available. Should such a relationship hold in future research, it will enable innovative, new ways of model evaluation based on much shorter timescales than the 20+ years typically used.

To test whether the results for the ICON model are merely an artefact of the logistic regression, we also use a more complex, but less interpretable CNN. The CNN classifiers achieve a similar overall accuracy of 99.7% for the same *dataset out-of-sample* framework and samples with the global mean removed. In general, the pattern of models with samples that get misclassified is quite consistent between the logistic regression and the CNN (figure 2a and b). While ICON still stands out as the model most likely to be confused for an observation, confirming the results from the last section, the CNN is able to correctly identify the majority (75.1%) of test samples, suggesting that it learns some more fundamental model properties that persist also at high resolution. Compared to the rather simple “model fingerprint” shown for the logistic regression in figure 1a, the classifications from the CNN are, thus, likely to be based on more complex relationships. We plan to investigate these relationships and the importance of different grid cells for the skill of the CNN in future work, drawing on techniques that, for example, aim to reveal regions of higher and lower importance in the temperature maps used as input [Bach et al., 2015].

3.4. Convolutional neural network classification of out-of-sample datasets without climatological bias

Based on these results, we, next, test if models and observations can still be separated in the absence of any climatological biases. To do this we now also remove the mean seasonal cycle from each sample (see section 2.3 for methodological details, figure S11 for the resulting multi-model mean bias equivalent to figure 1, and figure S12 for a breakdown by individual models). This means that any dataset specific, persistent regional biases that might have served as a basis for separation so far are now removed, along with any biases in the equator-pole gradient or between the hemispheres. Therefore, the classifiers can now only train on the spatial relationships of the remaining internal variability (which could be interpreted as daily weather), making the classification task considerably harder.

For this case, logistic regression no longer has any skill as the only remaining sources of information are non-linear relations between the spatial structures of daily global weather and the test samples are all centred around the decision threshold (not shown). In contrast, the CNN achieves an overall accuracy of about 94.2% demonstrating the power of this non-linear method. Figure 2c shows the corresponding breakdown of predicted probabilities revealing that now almost all models get confused for observations a number of times but still all are classified correctly for the vast majority of test samples, with the sole exception being the ICON model.

For ICON the seasonal cycle has been estimated using only the 31-day running window as only one year is available. This differs from the other datasets where the seasonal cycle has been calculated over the full 20 years of the training period (section 2.3). Therefore, the results for ICON need to be interpreted with care and should be revisited once more data are available. Nevertheless, we show these preliminary findings here, to highlight that, based on these results the structure of the remaining internal variability in ICON is recognised as more closely resembling observations than CMIP6 generation models. In fact, ICON is more frequently classified as observation than three of the four observational datasets (ERA5, MERRA2, and 20CR) by the respective classifiers trained with the tested dataset withheld. While this result is preliminary and not conclusive due to the limited amount of data available, it, again, points towards very encouraging properties of kilometre-scale models that warrant closer investigation as more data become available.

In turn, the DOISST dataset is identified correctly with perfect accuracy in all three cases shown in figure 2 with only individual misclassifications appearing even when bootstrapping the training data (figure S1). Optimistically interpreted, this could mean that the classifiers are picking up on the fact that DOISST is the dataset with the least amount of model included (see section 2.1) and that they have indeed learned some fundamental distinguishing features. This interpretation is supported by the fact that 20CR is most prone to get confused for a model, while also being the observational dataset that relies most heavily on a model for its output.

The overall skill of this binary classification of out-of-sample datasets is notable, in particular, when considering that bias correcting each model by subtracting the mean seasonal cycle and the daily

global mean effectively removes the entire time-persistent regional bias as well as any global mean offset between the datasets. This means that the only remaining sources of information to learn from are amplitude and spatial dependencies of the remaining daily temperature variability. One remaining source of model-observation differences for this case could arise from the coupling of atmosphere and ocean and the resulting surface energy balance in the models.

In a planned follow up study we will build on the results presented here and analyse the origin of this skill in more detail, using explainable machine learning techniques [e.g., [Bach et al., 2015](#)] as well as more specific approaches drawing on domain knowledge from climate sciences. The latter will include, for example, targeted masking of certain regions where climate models are known to perform particularly well/poorly to systematically investigate which areas of the globe are essential for skill and how this might depend on the models used. Such a combination of general and domain-specific approaches to classification skill is important to account for special properties of the temperature maps used compared to more general image classification. These include fundamental properties of the climate system such as the imprint of topography, temperature gradients, and circulation patterns, which are to some extent common to all datasets.

4. Identifying models by name

In the first part of the manuscript, we showed that there are common features across models and observations, respectively, that enable us to reliably identify even datasets unseen in training. In this section, we investigate whether there are also separating features that allow us to distinguish models from each other. Previous research, based on climatological timescales, has shown that models can be separated as well as clustered into families based only on their output [e.g., [Masson and Knutti, 2011](#), [Knutti et al., 2013](#), [Boé, 2018](#), [Brunner et al., 2020](#), [Merrifield et al., 2020, 2023](#)]. Here, we investigate whether models (and observations) still have unique features that allow them to be identified even on daily timescales.

We use the CNN on the data with the seasonal cycle and global mean removed and train it to recognise each of the 43 models as well as the four observational datasets. We increase the number of training samples to 2'000 per dataset for this case where we only train a single classifier. In the previous section the tested dataset was withheld from training, this is obviously no longer possible for this case where we aim to identify each model by name. Therefore we only use temporally out-of-sample test samples (see section 2.3 for details).

Assigning the correct label to each of the 47 datasets yields an overall accuracy of 83.4%. To put this into context, note that compared to the binary classification in the last section, we are now aiming to separate 47 categories, which considerably increases the difficulty of the classification. The CNN is thus able to pick up patterns unique to each dataset in order to separate it from all other datasets.

Figure 3 shows a breakdown of accuracy by dataset in a confusion matrix of true sample names versus the predicted sample names. Correct predictions (predicted name equals true name) are located on the main-diagonal of the matrix and use green shading. As expected from the overall accuracy, the majority of samples are assigned correctly with misclassifications exceeding 10% almost exclusively only found within model families. Such misclassifications between models from the same family are shown in purple shading and are mostly located in the secondary diagonals, as most related models have similar names and the models are ordered alphabetically.

Overall, the model with the highest number of correctly identified samples is MIROC-ES2L (99.9%), indicating that it is very different from all other models. This is consistent with studies using time averages over several decades to investigate model dependence in CMIP5 [[Knutti et al., 2013](#)] and CMIP6 [[Brunner et al., 2020](#)]. In turn, the models with the lowest number of correct predictions all belong to larger model families (models with less than 80% accuracy in figure 3). These results highlight that models can be separated by name on the basis of their pattern of daily internal variability and

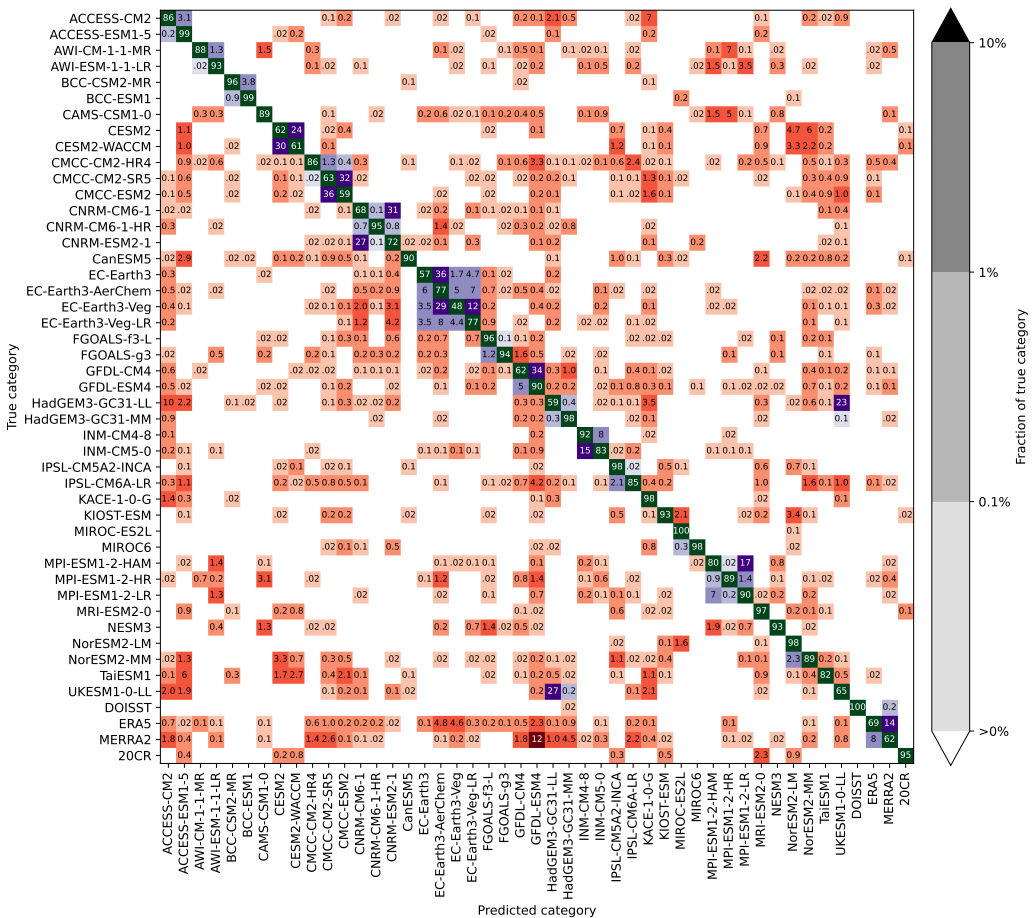


Figure 3. Confusion matrix showing the frequency of predicted versus true labels. The main diagonal shows correct predictions using green shading, purple shading indicates misclassifications within a model family (see table S3), and red shading indicates other misclassifications. Values are in % relative to the total number of samples in each category. The number in each box gives the value rounded to the last shown digit with rows not adding up to 100 % only due to rounding.

that overlaps in the models’ source code lead to similarities in their daily internal variability, resulting in a higher chance for misclassification within families.

On closer inspection, even some of the misclassifications outside of model families (red shading in figure 3) follow (more distant) model relationships. For example, about 10 % of samples from the UK’s HadGEM3-GC31-LL are misclassified as the Australian ACCESS-CM2 model (middle of first column in figure 3), which is probably due to the fact that ACCESS-CM2 reuses many of the UK models’ components [Bi et al., 2020]. Similarly, about 7 % of samples from ACCESS-CM2 are misclassified as the Korean KACE-1-0-G model (middle of first row in figure 3), which is also related to the HadGEM family [Lee et al., 2020]. Similar considerations apply to other related model groups (see, e.g., Brunner et al. [2020] for a discussion of broader model families), although there also remain a number of misclassifications that cannot be explained.

Similar to the binary case discussed in the first part, resolution (and related changes in the parametrizations) emerges as a property that is important for classification skill. For example, in the CMCC family the CM2-SR5 and ESM2 variants are confused with each other in about a third of the samples while the HR4 variant with a higher resolved ocean [Cherchi et al., 2019], is hardly confused with either of the former two, suggesting that the higher resolution sets the model apart. A somewhat similar pattern can be observed for the other three families with three or more members: EC-Earth (Veg-LR is less often confused with family members and has a lower atmospheric resolution; Döscher et al. [2022]), HadGEM (GC31-MM with higher atmospheric and ocean resolution; Andrews et al. [2019]), and MPI (HR with higher atmospheric and ocean resolution; Mauritsen et al. [2019]).

Concerning observations, a notable feature of figure 3 is that misclassifications between models and observations are not symmetric. Hardly any models are being misclassified for observations, while the observational datasets ERA5 and MERRA2 get confused as models for 20 % and 30 % of samples, respectively. This is consistent with the dataset out-of-sample results shown in figure 2c, where we found that observations are mistaken for models more often than vice-versa. A possible interpretation of this behaviour is that models produce more homogeneous patterns persistent across days (samples), while the two reanalyses in question produce more diverse output due the assimilation of observations. This will be further investigated in future work, including the identification of possible patterns in the misclassifications, for example a seasonality.

Similar to confusions between models, observational misclassifications may reflect potential (remote) dependencies in the source code even between models and reanalyses. For example, ERA5, which is predicted to be a model from the EC-Earth family for about 10 % of test samples, has documented dependencies on the ECMWF atmosphere which is also used in ERA5 [Döscher et al., 2022]. MERRA2 is predicted to be the GFDL-ESM4 model for about 12 % of cases, which might be attributable to common heritage as the atmospheric models used in GFDL-ESM4 (AM4.0; Dunne et al. [2020]) and MERRA2 (GEOS-5; Molod et al. [2015], Rienecker and Coauthors [2008]) are based on the same dynamical core [Lin, 2004].

The third observational dataset, DOISST, is never misclassified which is consistent with the results from the binary case presented in figure 2. The combination of these two results suggests that DOISST has very clear observational properties, but is still a very distinct dataset. For 20CR we find a slightly different behaviour to the binary case, with the number of misclassifications being considerably reduced in figure 4. This could mean that 20CR has properties of both model and observation, making it easier to identify it as an individual dataset rather than as belonging into the broader observational category.

Finally, we investigate how the daily differences between models relate to the differences due to global warming and check whether the classification remains robust in a changing climate by drawing test samples from the period 2091-2100 rather than from 2005-2014. There is no absolute warming present in either training or test samples due to the removal of the daily global mean, but daily weather patterns are expected to change significantly in a warming world [Sippel et al., 2020]. This is particularly true as we use data from the high-emission pathway SSP5-8.5 which leads to an additional global mean warming of about 4 K compared to today depending on the model [IPCC, 2021]. For this case only 33 models and no observations are available. As figure 4 shows the patterns learned by the CNN in the historical period still persist even after severe climate change and allow the correct identification of about 69.9 % of the test samples from the end of the century. For this case, several models have more than 10 % of their samples misclassified as another, not closely related model. Still, many of the characteristics discussed above persist for this case. For example, MIROC-ES2L remains the model with the highest accuracy and EC-Earth3-Veg remains the model with the most misclassified samples.

Ultimately, classifiers similar to the one used here, once trained, could be used, for example, in model development to investigate the impact of changes in parametrizations, resolution, or model components on the model output without the need to run the tested model for several decades. Conversely, if a model is no longer recognised in a future run this might also be an indication for potential problems warranting a closer investigation.

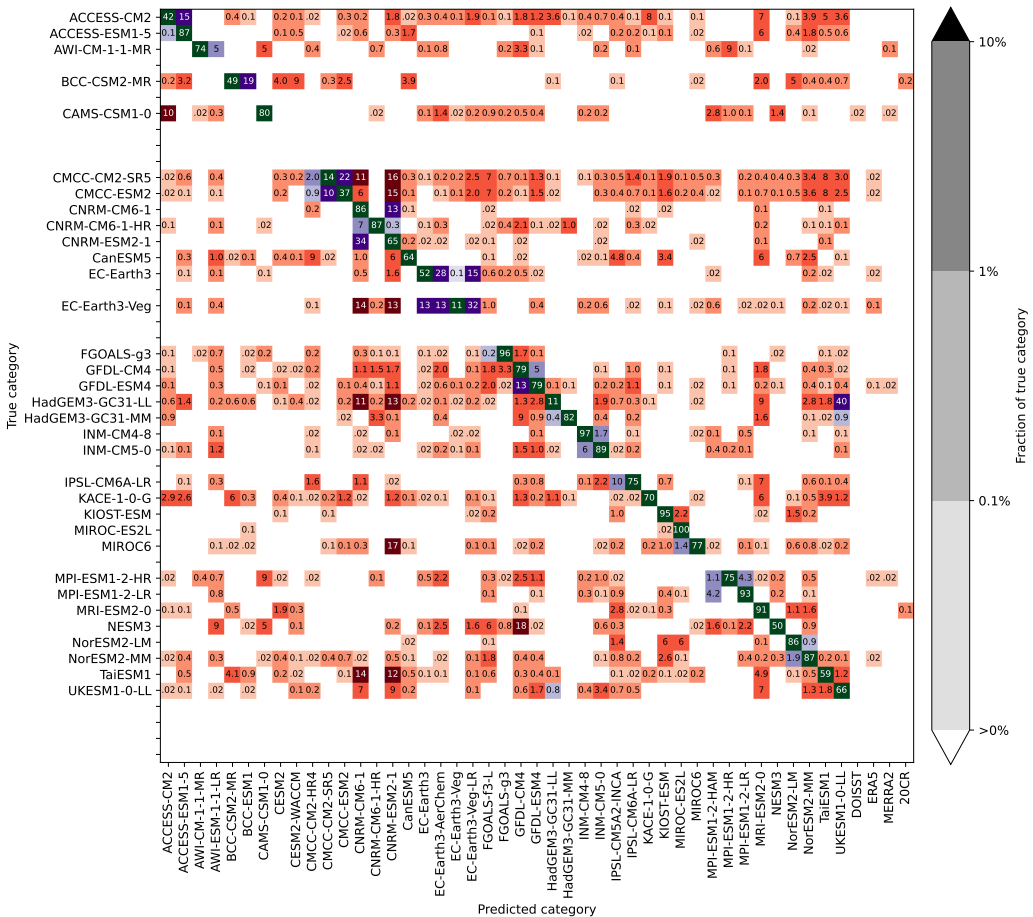


Figure 4. Same as figure 3 but with test data from the end of the century (2091-2100). Labels from datasets which do not cover this period are omitted in the true category.

5. Summary, conclusions, and outlook

We have shown that machine learning classifiers, once trained, can distinguish CMIP6 generation climate models from observations based on only the temperature map of a single day even for entirely new models never used in training. Both investigated approaches (logistic regression and convolutional neural network – CNN) were found to perform very well in separating 2 m surface air temperature fields where only the global mean has been removed, both achieving an accuracy of over 99 %. When the mean seasonal cycle was removed from each grid cell and dataset in addition, the logistic regression no longer showed any skill while the CNN still achieved an accuracy of over 90 %.

The performance for the latter case is quite remarkable, given that the removal of the mean seasonal cycle means that the classifiers could not learn from regions of dataset-specific, time-persistent biases, and thus had to rely only on the spatial dependence structures and the amplitudes of variations of daily global weather. The properties of the CNN as a highly non-linear, deep learning method, however, did not allow a straightforward extraction of the features used to separate the two categories, but a planned detailed investigation will be able to reveal more details in future work. This will be based, for example, on layer-wise relevance propagation, a technique that can reveal the “grid cell relevance”

of the temperature maps used as input for the output probabilities of a trained neural network [Bach et al., 2015, Toms et al., 2020, Labe and Barnes, 2022]. For a comprehensive overview of such an approach applied to a related problem, including a review of the current literature, see, for example Labe and Barnes [2022]. These techniques investigating the classifiers themselves will be combined with background knowledge about climate models to provide integrated and interpretable insights into the origins of the classification skill.

In addition to the CMIP6 models, we also tested the classifiers on one year of prototype data from a global, storm-resolving simulation run with ICON at a resolution of 5 km. The logistic regression classifiers were unable to clearly assign the samples from ICON into either category, indicating that this high-resolution case has different, and potentially reduced daily biases or more realistic covariance structure compared to the other, low-resolution CMIP6 models. The CNN, in turn, managed to correctly predict that the samples from ICON with only the global mean removed belong to the model category for slightly more than 75% of samples, which is still a much lower value than for all other models. In the case where the seasonal cycle (estimated from only one year of data) was removed as well, the CNN misclassified the vast majority of samples as clearly belonging into the observation category.

This case raises a number of interesting questions, that we will follow up upon once more data become available, for example: Does the emerging higher similarity between ICON and observations truly reflect improved modelled characteristics of the daily temperature field covariance structure, or could it be due to some compensating error phenomena? If the former, is the higher similarity to observations due to reduced biases overall, or due to improved daily covariance structure of temperature fields? Which resolution or other improvements would it take to truly pass the “climate model Turing test” [Palmer, 2016] of inseparability of output fields of observations and climate models? The result for ICON is potentially highly encouraging, but we warrant that a cautious interpretation is needed, as only a short ICON simulation period is available at present, and thus some effects of compensating errors cannot be definitely excluded.

In the second part of the study, we investigated the ability of the CNN to identify each of the 43 models and the four observational datasets included in the study by their name. Again, we used daily temperature fields with the mean seasonal cycle and the daily global mean removed. We found an overall accuracy of 83 %, which is about 40 times better than the baseline of a random choice. These results show that the CNN is clearly able to pick up relations between features that reliably separate models, including very similar variants from the same model families. At the same time, most of the misclassifications occur within model families or can be traced back to more distant “relations” such as common “ancestors”. There is evidence that this behaviour even holds for two of the reanalyses, ERA5 and MERRA2 which are misclassified as models from the EC-Earth and GFDL families, respectively, for more than 10 % of cases and have documented common ancestry. Although more in-depth research is needed to confirm these results, they provide an interesting finding about the imprint of shared code even on short timescales and between development streams that have diverged many years ago.

Finally, we showed that the CNN is able to correctly identify about 70 % of test samples even when they are drawn from the period 2091-2100 under the high-emission scenario SSP5-8.5, which is separated from the training period by about 100 years and features an about 4 K warmer climate in the global average. Although this mean warming itself is not included in the samples, weather patterns are expected to change considerably due to climate change [Sippel et al., 2020]. This means that the features used to identify climate models are –to a certain extent– state-invariant and thus remain robust even under a warming exceeding several degrees centigrade.

Future applications could build on the approaches illustrated here in several ways:

- They could add to the model evaluation toolbox [Eyring et al., 2019] and could target, for example, the classification of individual model components (e.g., atmospheric or ocean component), model generations (e.g., CMIP6 versus the roughly 10 years older CMIP5), perturbed parameter ensembles, or strains of model development in general. Following recent

work from [Labe and Barnes \[2022\]](#), misclassifications could also be used systematically to draw conclusions about model performance.

- The classification approaches could be used to pinpoint model-model or model-observation differences and similarities. This could be done by analysing the spatial scales of separability, that is, whether models on regional domains are less separable than globally, and/or whether this may depend on specific regions. Additionally, illustrating and understanding the patterns of separability, by using explainable neural network techniques [e.g., [Toms et al., 2020](#)] revealing how the neural network has learnt to distinguish models and observations, could provide additional insights.
- Related approaches could also be applied to infer model performance directly (e.g., predicting an estimate of climatological model error from short timescales) and possibly directly incorporating physical or dynamical processes (such as changes between two consecutive days) [[Kashinath et al., 2021](#)]. This may be particularly relevant for high-resolution simulations such as the storm-resolving simulations currently in development, for which only short periods of simulation are available. In addition, recent efforts to merge climate predictions initialised from an observed state seamlessly with climate projections [[Befort et al., 2022](#)], may be interesting to analyse with our method, as it allows to diagnose from short timescales at which point the climatological model biases start to emerge, which may provide an opportunity for model development [[Palmer, 2016](#)].
- Here we have focused on spatial patterns of mean temperature but other variables, such as precipitation, or other dimensions, such as the temporal distribution (potentially in a regional domain as discussed above) could also be considered to investigate their behaviour.
- Our approach tests to which degree transferring patterns and relationships between models and observations is justified [[Meinshausen, 2018](#)]. This assumption of distributional robustness is frequently made in the literature when classifiers are trained on simulated data and then applied to observed data [[Gibson et al., 2021](#), [Gordon et al., 2021](#), [Kadow et al., 2020](#), [Labe and Barnes, 2021](#), [Sippel et al., 2021](#)]. From this perspective our results can be seen as adversarial validation, which can be used to check whether the generalisation from training to test sets is justified on different timescales [[Shen et al., 2021](#)].
- Lastly, and most speculatively, recent advances in machine learning towards image-to-image translation, using, for instance, techniques such as generative adversarial networks [[Stengel et al., 2020](#)], could provide an avenue to iteratively bias-correct model output in relation to observations, until a hypothetical “bias-corrected” spatial pattern would be indistinguishable from observations. The idea in such generative adversarial approaches is precisely that a classifier cannot tell the difference between a simulated, “bias-corrected” output field, and an observed one.

Acknowledgements. The authors thank Reto Knutti, Erich M. Fischer and Christoph Schär (all at ETH Zurich), Aiko Voigt (University of Vienna), Bjorn Stevens (Max Planck Institute for Meteorology, Hamburg) and Michael Notter (EPFL, Lausanne) for valuable discussions and feedback on various aspects of the manuscript. We thank two anonymous reviewers for their helpful comments. We acknowledge the World Climate Research Programme, which, through its Working Group on Coupled Modelling, coordinated and promoted CMIP6. We thank the climate modeling groups for producing and making their model output available, the Earth System Grid Federation (ESGF) for archiving the data and providing access, and the multiple funding agencies that support CMIP6 and ESGF. This study was generated using Copernicus Climate Change Service information from ERA5. Support for the 20CR dataset used in this work is provided by the U.S. Department of Energy, Office of Science Biological and Environmental Research (BER), by the National Oceanic and Atmospheric Administration Climate Program Office, and by the NOAA Physical Sciences Laboratory. Many thanks to the nextGEMS project for providing the storm-resolving ICON runs, the NASA GMAO for providing MERRA2, NOAA for providing DOISST, and to Urs Beyerle for downloading the CMIP6 data used in this work.

Funding Statement. This research has been supported by the H2020 European Research Council project “European Climate Prediction System” (EUCP; grant no. 776613). S.S. acknowledges funding received from the Swiss National Science Foundation within the project “Combining theory with Big Data? The case of uncertainty in prediction of trends in extreme weather and impacts” (grant no. 167215), the Swiss Data Science Centre within the project “Data Science-informed attribution of changes in the Hydrological cycle” (DASH; C17-01) and within the European Union H2020 project “Artificial intelligence for detection and attribution” (XAIDA; grant no. 101003469).

Competing Interests. None.

Data Availability Statement. All data used in this study are freely available for research applications. Lists of all used CMIP6 models and observations are included in the supplement tables S1-S3.

Ethical Standards. The research meets all ethical guidelines, including adherence to the legal requirements of the study country.

Author Contributions. This work was conceptualised and written by L.B. with contributions from S.S.. Data acquisition, analysis, and visualisation by L.B.. Both authors approved the final submitted draft.

Supplementary Material. Supplementary material is available for this manuscript.

References

- Timothy Andrews, Martin B. Andrews, Alejandro Bodas-Salcedo, Gareth S. Jones, Till Kuhlbrodt, James Manners, Matthew B. Menary, Jeff Ridley, Mark A. Ringer, Alistair A. Sellar, Catherine A. Senior, and Yongming Tang. Forcings, Feedbacks, and Climate Sensitivity in HadGEM3-GC3.1 and UKESM1. *J. Adv. Model. Earth Syst.*, 11(12):4377–4394, 2019. ISSN 19422466. doi: 10.1029/2019MS001866.
- James D. Annan and Julia C. Hargreaves. On the meaning of independence in climate science. *Earth Syst. Dyn.*, 8(1):211–224, 2017. ISSN 21904987. doi: 10.5194/esd-8-211-2017.
- Sebastian Bach, Alexander Binder, Grégoire Montavon, Frederick Klauschen, Klaus Robert Müller, and Wojciech Samek. On pixel-wise explanations for non-linear classifier decisions by layer-wise relevance propagation. *PLoS One*, 10(7):1–46, 2015. ISSN 19326203. doi: 10.1371/journal.pone.0130140.
- Elizabeth A. Barnes, James W. Hurrell, Imme Ebert-Uphoff, Chuck Anderson, and David Anderson. Viewing Forced Climate Patterns Through an AI Lens. *Geophys. Res. Lett.*, 46(22):13389–13398, 2019. ISSN 19448007. doi: 10.1029/2019GL084944.
- Peter Bauer, Bjorn Stevens, and Wilco Hazeleger. A digital twin of Earth for the green transition. *Nat. Clim. Chang.*, 11(2):80–83, 2021. ISSN 17586798. doi: 10.1038/s41558-021-00986-y. URL <http://dx.doi.org/10.1038/s41558-021-00986-y>.
- D. J. Bafort, L. Brunner, L. F. Borchert, C. H. O’Reilly, J. Mignot, A. P. Ballinger, G. C. Hegerl, J. M. Murphy, and A. Weisheimer. Combination of Decadal Predictions and Climate Projections in Time: Challenges and Potential Solutions. *Geophys. Res. Lett.*, 49(15):1–18, 2022. ISSN 19448007. doi: 10.1029/2022GL098568.
- Daohua Bi, Martin Dix, Simon Marsland, Siobhan O’farrell, Arnold Sullivan, Roger Bodman, Rachel Law, Ian Harman, Jhan Sribnovsky, Harun A. Rashid, Peter Dobrohotoff, Chloe Mackallah, Hailin Yan, Anthony Hirst, Abhishek Savita, Fabio Boeira Dias, Matthew Woodhouse, Russell Fiedler, and Aidan Heerdegen. Configuration and spin-up of ACCESS-CM2, the new generation Australian Community Climate and Earth System Simulator Coupled Model. *J. South. Hemisph. Earth Syst. Sci.*, 70(1):225–251, 2020. ISSN 22065865. doi: 10.1071/ES19040.
- Craig H. Bishop and Gab Abramowitz. Climate model dependence and the replicate Earth paradigm. *Clim. Dyn.*, 41(3-4):885–900, 2013. ISSN 09307575. doi: 10.1007/s00382-012-1610-y.
- L. Bock, A. Lauer, M. Schlund, M. Barreiro, N. Bellouin, C. Jones, G. A. Meehl, V. Predoi, M. J. Roberts, and V. Eyring. Quantifying Progress Across Different CMIP Phases With the ESMValTool. *J. Geophys. Res. Atmos.*, 125(21):1–28, 2020. ISSN 21698996. doi: 10.1029/2019JD032321.
- Julien Boé. Interdependency in Multimodel Climate Projections: Component Replication and Result Similarity. *Geophys. Res. Lett.*, 45(6):2771–2779, mar 2018. ISSN 00948276. doi: 10.1002/2017GL076829. URL <http://doi.wiley.com/10.1002/2017GL076829>.
- Florent Brient, Romain Roehrig, and Aurore Voldoire. Evaluating Marine Stratocumulus Clouds in the CNRM-CM6-1 Model Using Short-Term Hindcasts. *J. Adv. Model. Earth Syst.*, 11(1):127–148, 2019. ISSN 19422466. doi: 10.1029/2018MS001461.

- Lukas Brunner, Angeline G. Pendergrass, Flavio Lehner, Anna L. Merrifield, Ruth Lorenz, and Reto Knutti. Reduced global warming from CMIP6 projections when weighting models by performance and independence. *Earth Syst. Dyn.*, 11(4):995–1012, nov 2020. ISSN 2190-4987. doi: 10.5194/esd-11-995-2020. URL <https://esd.copernicus.org/articles/11/995/2020/>.
- Rei Chemke, Laure Zanna, and Lorenzo M. Polvani. Identifying a human signal in the North Atlantic warming hole. *Nat. Commun.*, 11(1):1–7, 2020. ISSN 20411723. doi: 10.1038/s41467-020-15285-x. URL <http://dx.doi.org/10.1038/s41467-020-15285-x>.
- Guoxing Chen, Wei-Chyung Wang, Qing Bao, and Jiandong Li. Evaluation of Simulated Cloud Diurnal Variation in CMIP6 Climate Models. *J. Geophys. Res. Atmos.*, 127(6):1–14, 2022. ISSN 2169-897X. doi: 10.1029/2021jd036422.
- A. Cherchi, P. G. Fogli, T. Lovato, D. Peano, D. Iovino, S. Gualdi, S. Masina, E. Scoccimarro, S. Matera, A. Bellucci, and A. Navarra. Global Mean Climate and Main Patterns of Variability in the CMCC-CM2 Coupled Model. *J. Adv. Model. Earth Syst.*, 11(1):185–209, 2019. ISSN 19422466. doi: 10.1029/2018MS001369.
- Richard Davy and Stephen Outten. The Arctic Surface Climate in CMIP6: Status and Developments since CMIP5. *J. Clim.*, 33(18):8047–8068, sep 2020. ISSN 0894-8755. doi: 10.1175/JCLI-D-19-0990.1. URL <https://journals.ametsoc.org/view/journals/clim/33/18/jcliD190990.xml>.
- Iris De Vries, Sebastian Sippel, Angeline G Pendergrass, and Reto Knutti. Global detection of forced changes in mean and extreme precipitation is robust but observations disagree on the magnitude of change. *EGUsphere*, (July), 2022. doi: 10.5194/egusphere-2022-568.
- Ralf Döscher, Mario Acosta, Andrea Alessandri, Peter Anthoni, Thomas Arsouze, Tommi Bergman, Raffaele Bernardello, Souhail Boussetta, Louis-philippe Caron, Glenn Carver, Miguel Castrillo, Franco Catalano, Ivana Cvijanovic, Paolo Davini, Evelien Dekker, Francisco J. Doblas-Reyes, David Docquier, Pablo Echevarria, Uwe Fladrich, Ramon Fuentes-Franco, Matthias Gröger, Jost v. Hardenberg, Jenny Hieronymus, M. Pasha Karami, Jukka-Pekka Keskinen, Torben Koenigk, Risto Makkonen, François Massonnet, Martin Ménégoz, Paul A. Miller, Eduardo Moreno-Chamarro, Lars Nieradzick, Twan van Noije, Paul Nolan, Declan O’Donnell, Pirkka Ollinaho, Gijs van den Oord, Pablo Ortega, Oriol Tintó Prims, Arthur Ramos, Thomas Reerink, Clement Rousset, Yohan Ruprich-Robert, Philippe Le Sager, Torben Schmith, Roland Schrödner, Federico Serva, Valentina Sicardi, Marianne Sloth Madsen, Benjamin Smith, Tian Tian, Etienne Tourigny, Petteri Uotila, Martin Vancoppenolle, Shiyu Wang, David Wårlind, Ulrika Willén, Klaus Wyser, Shuting Yang, Xavier Yepes-Arbós, and Qiong Zhang. The EC-Earth3 Earth system model for the Coupled Model Intercomparison Project 6. *Geosci. Model Dev.*, 15(7):2973–3020, apr 2022. ISSN 1991-9603. doi: 10.5194/gmd-15-2973-2022. URL <https://gmd.copernicus.org/articles/15/2973/2022/>.
- J. P. Dunne, L. W. Horowitz, A. J. Adcroft, P. Ginoux, I. M. Held, J. G. John, J. P. Krasting, S. Malyshev, V. Naik, F. Paulot, E. Shevliakova, C. A. Stock, N. Zadeh, V. Balaji, C. Blanton, K. A. Dunne, C. Dupuis, J. Durachta, R. Dussin, P. P.G. Gauthier, S. M. Griffies, H. Guo, R. W. Hallberg, M. Harrison, J. He, W. Hurlin, C. McHugh, R. Menzel, P. C.D. Milly, S. Nikonov, D. J. Paynter, J. Ploshay, A. Radhakrishnan, K. Rand, B. G. Reichl, T. Robinson, D. M. Schwarzkopf, L. T. Sentman, S. Underwood, H. Vahlenkamp, M. Winton, A. T. Wittenberg, B. Wyman, Y. Zeng, and M. Zhao. The GFDL Earth System Model Version 4.1 (GFDL-ESM 4.1): Overall Coupled Model Description and Simulation Characteristics. *J. Adv. Model. Earth Syst.*, 12(11):1–56, 2020. ISSN 19422466. doi: 10.1029/2019MS002015.
- Veronika Eyring, Sandrine Bony, Gerald A. Meehl, Catherine A. Senior, Bjorn Stevens, Ronald J. Stouffer, and Karl E. Taylor. Overview of the Coupled Model Intercomparison Project Phase 6 (CMIP6) experimental design and organization. *Geosci. Model Dev.*, 9(5):1937–1958, may 2016. ISSN 1991-9603. doi: 10.5194/gmd-9-1937-2016. URL <https://www.geosci-model-dev.net/9/1937/2016/>.
- Veronika Eyring, Peter M. Cox, Gregory M. Flato, Peter J. Gleckler, Gab Abramowitz, Peter Caldwell, William D. Collins, Bettina K. Gier, Alex D. Hall, Forrest M. Hoffman, George C. Hurtt, Alexandra Jahn, Chris D. Jones, Stephen A. Klein, John P. Krasting, Lester Kwiatkowski, Ruth

- Lorenz, Eric Maloney, Gerald A. Meehl, Angeline G. Pendergrass, Robert Pincus, Alex C. Ruane, Joellen L. Russell, Benjamin M. Sanderson, Benjamin D. Santer, Steven C. Sherwood, Isla R. Simpson, Ronald J. Stouffer, and Mark S. Williamson. Taking climate model evaluation to the next level. *Nat. Clim. Chang.*, 9(2):102–110, 2019. ISSN 17586798. doi: 10.1038/s41558-018-0355-y. URL <http://dx.doi.org/10.1038/s41558-018-0355-y>.
- Ronald Gelaro, Will McCarty, Max J. Suárez, Ricardo Todling, Andrea Molod, Lawrence Takacs, Cynthia A. Randles, Anton Darmenov, Michael G. Bosilovich, Rolf Reichle, Krzysztof Wargan, Lawrence Coy, Richard Cullather, Clara Draper, Santha Akella, Virginie Buchard, Austin Conaty, Arlindo M. da Silva, Wei Gu, Gi Kong Kim, Randal Koster, Robert Lucchesi, Dagmar Merkova, Jon Eric Nielsen, Gary Partyka, Steven Pawson, William Putman, Michele Rienecker, Siegfried D. Schubert, Meta Sienkiewicz, and Bin Zhao. The modern-era retrospective analysis for research and applications, version 2 (MERRA-2). *J. Clim.*, 30(14):5419–5454, 2017. ISSN 08948755. doi: 10.1175/JCLI-D-16-0758.1.
- Peter B. Gibson, William E. Chapman, Alphan Altinok, Luca Delle Monache, Michael J. DeFlorio, and Duane E. Waliser. Training machine learning models on climate model output yields skillful interpretable seasonal precipitation forecasts. *Commun. Earth Environ.*, 2(1), 2021. ISSN 26624435. doi: 10.1038/s43247-021-00225-4. URL <http://dx.doi.org/10.1038/s43247-021-00225-4>.
- Filippo Giorgi and Erika Coppola. Does the model regional bias affect the projected regional climate change? An analysis of global model projections: A letter. *Clim. Change*, 100(3):787–795, 2010. ISSN 01650009. doi: 10.1007/s10584-010-9864-z.
- GMAO. MERRA-2 tavg1_2d_slv_Nx: 2d,1-Hourly,Time-Averaged,Single-Level,Assimilation,Single-Level Diagnostics V5.12.4, 2015.
- Emily M. Gordon, Elizabeth A. Barnes, and James W. Hurrell. Oceanic Harbingers of Pacific Decadal Oscillation Predictability in CESM2 Detected by Neural Networks. *Geophys. Res. Lett.*, 48(21), 2021. ISSN 0094-8276. doi: 10.1029/2021gl095392.
- Trevor Hastie, Robert Tibshirani, and Jerome Friedman. *The Elements of Statistical Learning*. Springer, 2 edition, mar 2009. ISBN 9780387848570. doi: 10.1080/01443610062940. URL <http://www.springerlink.com/index/D7X7KX6772HQ2135.pdf><http://www.ncbi.nlm.nih.gov/pubmed/15512507>.
- Hans Hersbach, Bill Bell, Paul Berrisford, Shoji Hirahara, András Horányi, Joaquín Muñoz-Sabater, Julien Nicolas, Carole Peubey, Raluca Radu, Dinand Schepers, Adrian Simmons, Cornel Soci, Saleh Abdalla, Xavier Abellan, Gianpaolo Balsamo, Peter Bechtold, Gionata Biavati, Jean Bidlot, Massimo Bonavita, Giovanna De Chiara, Per Dahlgren, Dick Dee, Michail Diamantakis, Rossana Dragani, Johannes Flemming, Richard Forbes, Manuel Fuentes, Alan Geer, Leo Haimberger, Sean Healy, Robin J. Hogan, Elías Hólm, Marta Janisková, Sarah Keeley, Patrick Laloyaux, Philippe Lopez, Cristina Lupu, Gabor Radnoti, Patricia de Rosnay, Iryna Rozum, Freja Vamborg, Sebastien Villaume, and Jean Noël Thépaut. The ERA5 global reanalysis. *Q. J. R. Meteorol. Soc.*, 146(730):1999–2049, 2020. ISSN 1477870X. doi: 10.1002/qj.3803.
- Nagio Hirota, Yukari N. Takayabu, Masahiro Watanabe, and Masahide Kimoto. Precipitation reproducibility over tropical oceans and its relationship to the double ITCZ problem in CMIP3 and MIROC5 climate models. *J. Clim.*, 24(18):4859–4873, 2011. ISSN 08948755. doi: 10.1175/2011JCLI4156.1.
- Cathy Hohenegger, Peter Korn, Leonidas Linardakis, René Redler, Reiner Schnur, Panagiotis Adamidis, Jiawei Bao, Swantje Bastin, Milad Behraves, Martin Bergemann, Joachim Biercamp, Hendryk Bockelmann, Renate Brokopf, Nils Brüggemann, Lucas Casaroli, Fatemeh Chegini, George Datsieris, Monika Esch, Geet George, Marco Giorgetta, Oliver Gutjahr, Helmuth Haak, Moritz Hanke, Tatiana Ilyina, Thomas Jahns, Johann Jungclaus, Marcel Kern, Daniel Klocke, Lukas Kluft, Tobias Kölling, Luis Kornbluh, Sergey Kosukhin, Clarissa Kroll, Junhong Lee, Thorsten Mauritsen, Carolin Mehlmann, Theresa Mieslinger, Ann Kristin Naumann, Laura Paccini, Angel Peinado, Divya Sri Praturi, Dian Putrasahan, Sebastian Rast, Thomas Riddick, Niklas Roeber, Hauke Schmidt, Uwe Schulzweida, Florian Schütte, Hans Segura, Radomyra Shevchenko, Vikram Singh,

- Mia Specht, Claudia Christine Stephan, Raphaela Vogel, Christian Wengel, Marius Winkler, Florian Ziemer, Jochem Marotzke, and Bjorn Stevens. ICON-Sapphire : simulating the components of the Earth System and their interactions at kilometer and subkilometer scales. *Geosci. Model Dev.*, 2022. doi: 10.5194/gmd-2022-171. URL <https://doi.org/10.5194/gmd-2022-171>.
- William W. Hsieh. Evolution of machine learning in environmental science—A perspective. *Environ. Data Sci.*, 1:1–8, 2022. doi: 10.1017/eds.2022.2.
- Boyin Huang, Chunying Liu, Viva Banzon, Eric Freeman, Garrett Graham, Bill Hankins, Tom Smith, and Huai Min Zhang. Improvements of the Daily Optimum Interpolation Sea Surface Temperature (DOISST) Version 2.1. *J. Clim.*, 34(8):2923–2939, 2021. ISSN 08948755. doi: 10.1175/JCLI-D-20-0166.1.
- IPCC. Summary for Policymakers. In: Climate Change 2021: The Physical Science Basis. Contribution of Working Group I to the Sixth Assessment Report of the Intergovernmental Panel on Climate Change. 2021.
- Christopher Kadow, David Matthew Hall, and Uwe Ulbrich. Artificial intelligence reconstructs missing climate information. *Nat. Geosci.*, 13(6):408–413, 2020. ISSN 17520908. doi: 10.1038/s41561-020-0582-5. URL <http://dx.doi.org/10.1038/s41561-020-0582-5>.
- K. Kashinath, M. Mustafa, A. Albert, J. L. Wu, C. Jiang, S. Esmailzadeh, K. Azizzadenesheli, R. Wang, A. Chattopadhyay, A. Singh, A. Manepalli, D. Chirila, R. Yu, R. Walters, B. White, H. Xiao, H. A. Tchelepi, P. Marcus, A. Anandkumar, P. Hassanzadeh, and Prabhat. Physics-informed machine learning: Case studies for weather and climate modelling. *Philos. Trans. R. Soc. A Math. Phys. Eng. Sci.*, 379(2194), 2021. ISSN 1364503X. doi: 10.1098/rsta.2020.0093.
- Paul Keil, Thorsten Mauritsen, Johann Jungclaus, Christopher Hedemann, Dirk Olonscheck, and Rohit Ghosh. Multiple drivers of the North Atlantic warming hole. *Nat. Clim. Chang.*, 10(7):667–671, 2020. ISSN 17586798. doi: 10.1038/s41558-020-0819-8. URL <http://dx.doi.org/10.1038/s41558-020-0819-8>.
- Reto Knutti. The end of model democracy? *Clim. Change*, 102(3-4):395–404, oct 2010. ISSN 0165-0009. doi: 10.1007/s10584-010-9800-2. URL <http://link.springer.com/10.1007/s10584-010-9800-2>.
- Reto Knutti, David Masson, and Andrew Gettelman. Climate model genealogy: Generation CMIP5 and how we got there. *Geophys. Res. Lett.*, 40(6):1194–1199, mar 2013. ISSN 00948276. doi: 10.1002/grl.50256. URL <http://doi.wiley.com/10.1002/grl.50256>.
- Zachary M. Labe and Elizabeth A. Barnes. Detecting Climate Signals Using Explainable AI With Single-Forcing Large Ensembles. *J. Adv. Model. Earth Syst.*, 13(6), 2021. ISSN 19422466. doi: 10.1029/2021MS002464.
- Zachary M. Labe and Elizabeth A. Barnes. Comparison of Climate Model Large Ensembles With Observations in the Arctic Using Simple Neural Networks. *Earth Sp. Sci.*, 9(7), 2022. ISSN 23335084. doi: 10.1029/2022EA002348.
- Johan Lee, Jinwon Jisun Kim, Min Ah Sun, Byeong Hyeon Kim, Hyejin Moon, Hyun Min Sung, Jinwon Jisun Kim, and Young Hwa Byun. Evaluation of the Korea Meteorological Administration Advanced Community Earth-System model (K-ACE). *Asia-Pacific J. Atmos. Sci.*, 56(3):381–395, 2020. ISSN 19767951. doi: 10.1007/s13143-019-00144-7.
- Gen Li and Shang Ping Xie. Tropical biases in CMIP5 multimodel ensemble: The excessive equatorial pacific cold tongue and double ITCZ problems. *J. Clim.*, 27(4):1765–1780, 2014. ISSN 08948755. doi: 10.1175/JCLI-D-13-00337.1.
- Shian Jiann Lin. A "vertically Lagrangian" finite-volume dynamical core for global models. *Mon. Weather Rev.*, 132(10):2293–2307, 2004. ISSN 00270644. doi: 10.1175/1520-0493(2004)132<2293:AVLFDC>2.0.CO;2.
- Hsi Yen Ma, S. Xie, S. A. Klein, K. D. Williams, J. S. Boyle, S. Bony, H. Douville, S. Fermepin, B. Medeiros, S. Tyteca, M. Watanabe, and D. Williamson. On the correspondence between mean forecast errors and climate errors in CMIP5 models. *J. Clim.*, 27(4):1781–1798, 2014. ISSN 08948755. doi: 10.1175/JCLI-D-13-00474.1.

- D. Masson and R. Knutti. Climate model genealogy. *Geophys. Res. Lett.*, 38(8):1–4, 2011. ISSN 00948276. doi: 10.1029/2011GL046864.
- Thorsten Mauritsen, Jürgen Bader, Tobias Becker, Jörg Behrens, Matthias Bittner, Renate Brokopf, Victor Brovkin, Martin Claussen, Traute Crueger, Monika Esch, Irina Fast, Stephanie Fiedler, Dagmar Fläschner, Veronika Gayler, Marco Giorgetta, Daniel S. Goll, Helmuth Haak, Stefan Hagemann, Christopher Hedemann, Cathy Hohenegger, Tatiana Ilyina, Thomas Jahns, Diego Jimenez-de-la Cuesta, Johann Jungclaus, Thomas Kleinen, Silvia Kloster, Daniela Kracher, Stefan Kinne, Deike Kleberg, Gitta Lasslop, Luis Kornbluh, Jochem Marotzke, Daniela Matei, Katharina Meraner, Uwe Mikolajewicz, Kameswarrao Modali, Benjamin Möbis, Wolfgang A. Müller, Julia E.M.S. Nabel, Christine C.W. Nam, Dirk Notz, Sarah Sylvia Nyawira, Hanna Paulsen, Karsten Peters, Robert Pincus, Holger Pohlmann, Julia Pongratz, Max Popp, Thomas Jürgen Raddatz, Sebastian Rast, Rene Redler, Christian H. Reick, Tim Rohrschneider, Vera Schemann, Hauke Schmidt, Reiner Schnur, Uwe Schulzweida, Katharina D. Six, Lukas Stein, Irene Stemmler, Bjorn Stevens, Jin Song von Storch, Fangxing Tian, Aiko Voigt, Philipp Vrese, Karl Hermann Wieners, Stiig Wilkenskjeld, Alexander Winkler, and Erich Roeckner. Developments in the MPI-M Earth System Model version 1.2 (MPI-ESM1.2) and Its Response to Increasing CO₂. *J. Adv. Model. Earth Syst.*, 11(4):998–1038, 2019. ISSN 19422466. doi: 10.1029/2018MS001400.
- Gerald A. Meehl, Jadwiga H. Richter, Haiyan Teng, Antonietta Capotondi, Kim Cobb, Francisco Doblas-Reyes, Markus G. Donat, Matthew H. England, John C. Fyfe, Weiqing Han, Hyemi Kim, Ben P. Kirtman, Yochanan Kushnir, Nicole S. Lovenduski, Michael E. Mann, William J. Merryfield, Veronica Nieves, Kathy Pegion, Nan Rosenbloom, Sara C. Sanchez, Adam A. Scaife, Doug Smith, Aneesh C. Subramanian, Lantao Sun, Diane Thompson, Caroline C. Ummenhofer, and Shang Ping Xie. Initialized Earth System prediction from subseasonal to decadal timescales. *Nat. Rev. Earth Environ.*, 2(5):340–357, 2021. ISSN 2662138X. doi: 10.1038/s43017-021-00155-x.
- Malte Meinshausen, Zebedee R. J. Nicholls, Jared Lewis, Matthew J. Gidden, Elisabeth Vogel, Mandy Freund, Urs Beyerle, Claudia Gessner, Alexander Nauels, Nico Bauer, Josep G. Canadell, John S. Daniel, Andrew John, Paul B. Krummel, Gunnar Luderer, Nicolai Meinshausen, Stephen A. Montzka, Peter J. Rayner, Stefan Reimann, Steven J. Smith, Marten van den Berg, Guus J. M. Velders, Martin K. Vollmer, and Ray H. J. Wang. The shared socio-economic pathway (SSP) greenhouse gas concentrations and their extensions to 2500. *Geosci. Model Dev.*, 13(8):3571–3605, aug 2020. ISSN 1991-9603. doi: 10.5194/gmd-13-3571-2020. URL <https://gmd.copernicus.org/articles/13/3571/2020/>.
- Nicolai Meinshausen. CAUSALITY from A DISTRIBUTIONAL ROBUSTNESS POINT of VIEW. *2018 IEEE Data Sci. Work. DSW 2018 - Proc.*, (1):6–10, 2018. doi: 10.1109/DSW.2018.8439889.
- Anna L Merrifield, Lukas Brunner, Ruth Lorenz, Vincent Humphrey, and Reto Knutti. Climate model Selection by Independence , Performance , and Spread (ClimSIPS) for regional applications. (February):1–49, 2023. doi: 10.5194/egusphere-2022-1520.
- Anna Louise Merrifield, Lukas Brunner, Ruth Lorenz, Iselin Medhaug, and Reto Knutti. An investigation of weighting schemes suitable for incorporating large ensembles into multi-model ensembles. *Earth Syst. Dyn.*, 11(3):807–834, sep 2020. ISSN 2190-4987. doi: 10.5194/esd-11-807-2020. URL <https://esd.copernicus.org/articles/11/807/2020/>.
- A. Molod, L. Takacs, M. Suarez, and J. Bacmeister. Development of the GEOS-5 atmospheric general circulation model: Evolution from MERRA to MERRA2. *Geosci. Model Dev.*, 8(5):1339–1356, 2015. ISSN 19919603. doi: 10.5194/gmd-8-1339-2015.
- Dirk Notz and Simip Community. Arctic Sea Ice in CMIP6. *Geophys. Res. Lett.*, 47(10):1–11, 2020. ISSN 19448007. doi: 10.1029/2019GL086749.
- T. N. Palmer. A personal perspective on modelling the climate system. *Proc. R. Soc. A Math. Phys. Eng. Sci.*, 472(2188), 2016. ISSN 14712946. doi: 10.1098/rspa.2015.0772.
- Thomas Rackow, Nils Wedi, Kristian Mogensen, Peter Dueben, Helge F Goessling, Christian Kühnlein, Lorenzo Zampieri, and Thomas Jung. DYAMOND-II simulations with IFS-FESOM2, 2021.

- M. M. Rienecker and Coauthors. The GEOS-5 Data Assimilation System—Documentation of versions 5.0.1 and 5.1.0, and 5.2.0. *NASA Tech. Rep. Ser. Glob. Model. Data Assim. NASA/TM-2008-104606*, 27(December):92pp, 2008.
- Zheyang Shen, Jiashuo Liu, Yue He, Xingxuan Zhang, Renzhe Xu, Han Yu, and Peng Cui. Towards Out-Of-Distribution Generalization: A Survey. 14(8):1–22, 2021. URL <http://arxiv.org/abs/2108.13624>.
- Sebastian Sippel, Nicolai Meinshausen, Erich M Fischer, Enikő Székely, and Reto Knutti. Climate change now detectable from any single day of weather at global scale. *Nat. Clim. Chang.*, 10(1):35–41, jan 2020. ISSN 1758-678X. doi: 10.1038/s41558-019-0666-7. URL <http://dx.doi.org/10.1038/s41558-019-0666-7><http://www.nature.com/articles/s41558-019-0666-7>.
- Sebastian Sippel, Nicolai Meinshausen, Enikő Székely, Erich Fischer, Angeline G. Pendergrass, Flavio Lehner, and Reto Knutti. Robust detection of forced warming in the presence of potentially large climate variability. *Sci. Adv.*, 7(43):1–18, 2021. ISSN 23752548. doi: 10.1126/sciadv.abh4429.
- L. C. Slivinski, G. P. Compo, P. D. Sardeshmukh, J. S. Whitaker, C. McColl, R. J. Allan, P. Brohan, X. Yin, C. A. Smith, L. J. Spencer, R. S. Vose, M. Rohrer, R. P. Conroy, D. C. Schuster, J. J. Kennedy, L. Ashcroft, S. Brönnimann, M. Brunet, D. Camuffo, R. Cornes, T. A. Cram, F. Domínguez-Castro, J. E. Freeman, J. Gergis, E. Hawkins, P. D. Jones, H. Kubota, T. C. Lee, A. M. Lorrey, J. Luterbacher, C. J. Mock, R. K. Przybylak, C. Pudmenzky, V. C. Slonosky, B. Tinz, B. Trewin, X. L. Wang, C. Wilkinson, K. Wood, and P. Wyszynski. An evaluation of the performance of the twentieth century reanalysis version 3. *J. Clim.*, 34(4):1417–1438, 2021. ISSN 08948755. doi: 10.1175/JCLI-D-20-0505.1.
- Karen Stengel, Andrew Glaws, Dylan Hettinger, and Ryan N. King. Adversarial super-resolution of climatological wind and solar data. *Proc. Natl. Acad. Sci. U. S. A.*, 117(29):16805–16815, 2020. ISSN 10916490. doi: 10.1073/pnas.1918964117.
- Claudia Tebaldi and Reto Knutti. The use of the multi-model ensemble in probabilistic climate projections. *Philos. Trans. R. Soc. A Math. Phys. Eng. Sci.*, 365(1857):2053–2075, 2007. ISSN 1364-503X. doi: 10.1098/rsta.2007.2076. URL <http://rsta.royalsocietypublishing.org/cgi/doi/10.1098/rsta.2007.2076>.
- Baijun Tian and Xinyu Dong. The Double-ITCZ Bias in CMIP3, CMIP5, and CMIP6 Models Based on Annual Mean Precipitation. *Geophys. Res. Lett.*, 47(8):1–11, 2020. ISSN 19448007. doi: 10.1029/2020GL087232.
- Benjamin A. Toms, Elizabeth A. Barnes, and Imme Ebert-Uphoff. Physically Interpretable Neural Networks for the Geosciences: Applications to Earth System Variability. *J. Adv. Model. Earth Syst.*, 12(9):1–20, 2020. ISSN 19422466. doi: 10.1029/2019MS002002.
- Keith D. Williams, A. Bodas-Salcedo, M. Déqué, S. Fermepin, B. Medeiros, M. Watanabe, C. Jakob, S. A. Klein, C. A. Senior, and D. L. Williamson. The transpose-AMIP II experiment and its application to the understanding of southern ocean cloud biases in climate models. *J. Clim.*, 26(10):3258–3274, 2013. ISSN 08948755. doi: 10.1175/JCLI-D-12-00429.1.

RESEARCH ARTICLE

Supplement: Identifying climate models based on their daily output using machine learning

Lukas Brunner¹ * and Sebastian Sippel² 

¹Department of Meteorology and Geophysics, University of Vienna, Vienna, Austria

²Institute for Atmospheric and Climate Science, ETH Zurich, Zurich, Switzerland

*Corresponding author. Email: l.brunner@univie.ac.at

S1. Overview

- Section S2: Technical details and CNN layout
- Section S3: Bootstrap testing
- Section S4: Training evolution and test reliability of the CNN
- Section S6: Additional temperature maps
- Section S6: Models used and model families

Table S1. Overview of classifiers, classification type, bias corrections, out-of-sample frameworks, and presented results.

Classifier	Type	Bias correction	Out-of-sample	Results
Log. reg.	Binary	global mean	temporal	Fig 1a
Log. reg.	Binary	global mean	temporal and dataset	Fig 2a
Log. reg.	Binary	global mean	temporal ⁽¹⁾	Fig S1a
CNN	Binary	global mean	temporal and dataset	Fig 2b
CNN	Binary	seasonal cycle and global mean	temporal and dataset	Fig 2c
CNN	Binary	seasonal cycle and global mean	temporal ⁽¹⁾	Fig S1b
CNN	Multi-class	seasonal cycle and global mean	temporal	Fig 3
CNN	Mult-class	seasonal cycle and global mean	temporal ⁽²⁾	Fig 4

⁽¹⁾ Training data from 100 random bootstrap samples

⁽²⁾ Using test samples from the end-of-century period 2091-2100

S2. Technical details and CNN layout

We train the classifiers on a full node of the University of Vienna Institute for Meteorology and Geophysics *Jet* Linux cluster. It has 40 Intel Xeon Gold 6148 CPUs with 2.40GHz and a total of 755GB of memory. The logistic regression classifier is implemented using Python's scikit-learn library (<https://scikit-learn.org>), the convolutional neural network is implemented using tensorflow's keras library (<https://keras.io/>). Table S3 details the layers of the convolutional neural network used.

Table S2. Summary of layers for the convolutional neural network. The convolutional layers use the rectified linear unit as activation function, the dense layer uses softmax.

Layer	Properties	Output shape	Nr. parameters
Input	-	(72, 144, 1)	0
Convolutional	Depth: 128; Size: 5; Strides: 2	(36, 72, 128)	3'328
Max. pooling	Size: 4	(9, 18, 128)	0
Convolutional	Depth: 64; Size: 3; Strides: 1	(9, 18, 64)	73'792
Max. pooling	Size: 2	(4, 9, 64)	0
Convolutional	Depth: 64; Size: 3; Strides: 1	(4, 9, 64)	36'928
Max. pooling	Size: 2	(2, 4, 64)	0
Convolutional	Depth: 32; Size: 2; Strides: 1	(4, 9, 32)	8'224
Max. pooling	Size: 2	(1, 2, 32)	0
Flatten	-	(64)	0
Dense	-	(2 / 47)	130 / 3'055

S3. Bootstrap testing

In the main manuscript each classifier is trained on one realisation of randomly drawn training samples. To investigate the robustness of the results under different training samples we perform two bootstrap tests, one for the logistic regression classifier and one for the convolutional neural network. For both cases the classifier is trained on all models (i.e., the test samples are only temporally out-of-sample) as training individual classifiers for each model in addition to bootstrapping is computationally not feasible.

For both cases we re-train the classifier 100 times, based on the random bootstrap samples. Figure S1 shows the distribution of probabilities for the test samples from each model similar to figure 2 in the main manuscript. For the logistic regression classifier only the minimum/maximum range is affected by the bootstrapping (green uncertainty ranges), indicating that the method is mostly robust when using different training samples. For the convolutional neural network the interquartile range can also be somewhat affected when basing training on different samples. However, the uncertainty is overall rather small and does not change any of the conclusions from the main paper.

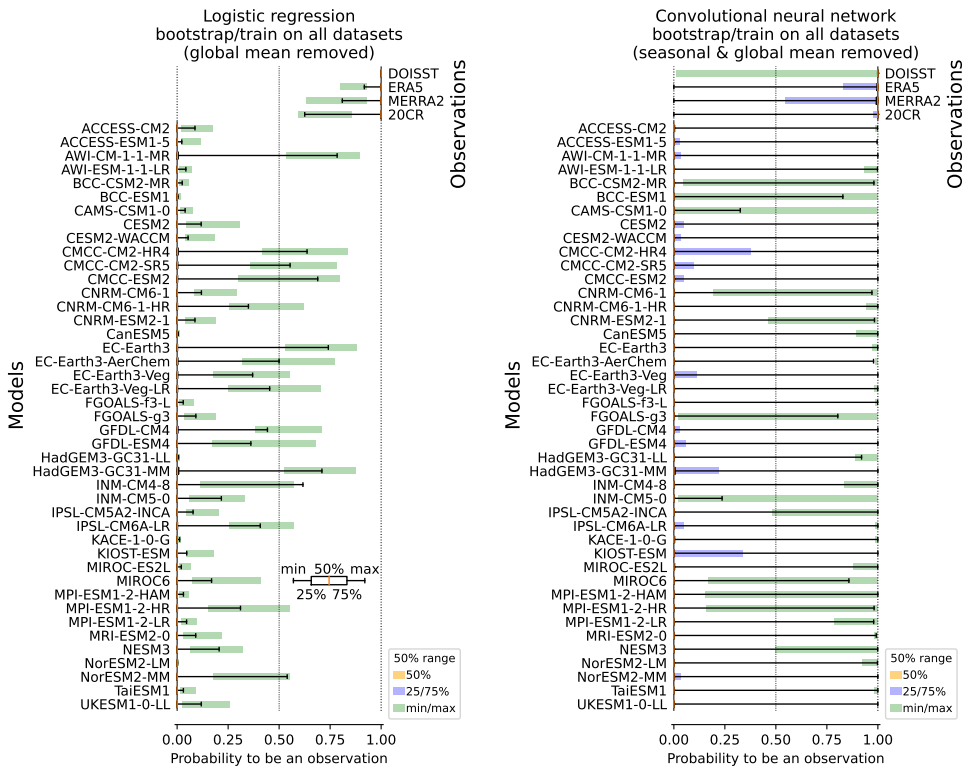


Figure S1. Distribution of predicted probabilities for the test set in a bootstrap setting. One bootstrap sample is plotted as boxes similar to figure 2 in the main manuscript. The shadings give the 50% uncertainty range in the total range (green), the interquartile range (blue), and the median (yellow). Note that the median uncertainty does not show in any case. (left) Results for a logistic regression classifier using data with the global mean removed. (right) Results for a convolutional neural network using data with the mean seasonal cycle and the global mean removed.

S4. Training evolution and test reliability of the CNN

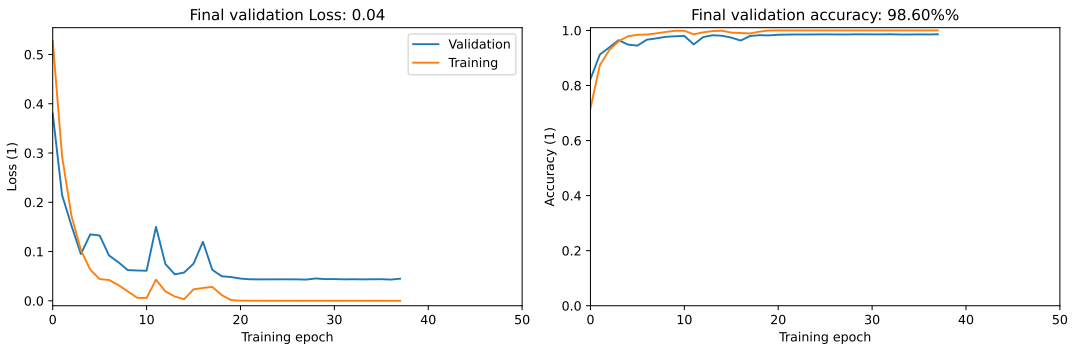


Figure S2. Training and validation loss (left) and accuracy (right) evolution of the convolutional neural network during the training process for separating models and observations with the seasonal mean cycle and the global mean removed. Training is interrupted before the maximum of 50 epochs by the use of an early stopping algorithm monitoring validation loss.

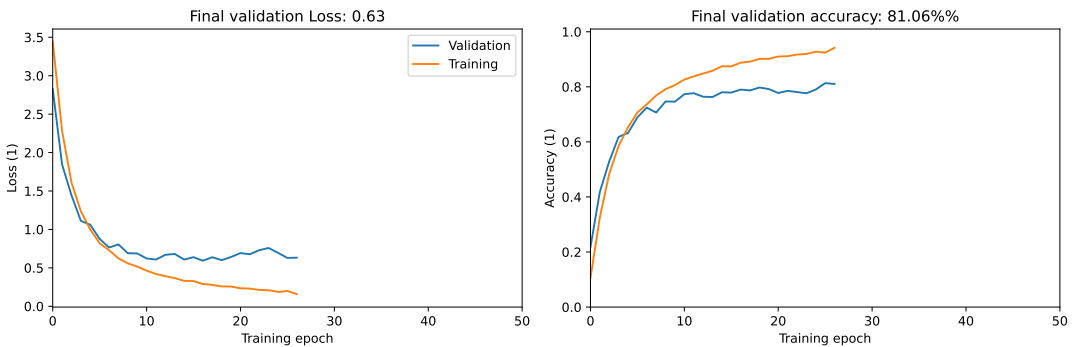


Figure S3. Similar to figure S2 but for the training process of separating 47 datasets.

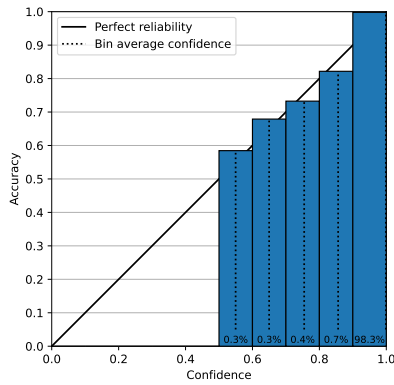


Figure S4. Reliability diagram for the logistic regression classifiers used in figure 2a. The x-axis is binned by the confidence assigned to the samples, the numbers at the bottom of each bar give the fraction of samples within each bin, and the dashed vertical lines give the average of all confidence values within each bin. The y-axis gives the average accuracy across samples in each bin (i.e., correct samples divided by total samples). For perfect reliability the average confidence should be equal to the average accuracy (i.e., the vertical dashed lines should coincide with the solid 1:1 line).

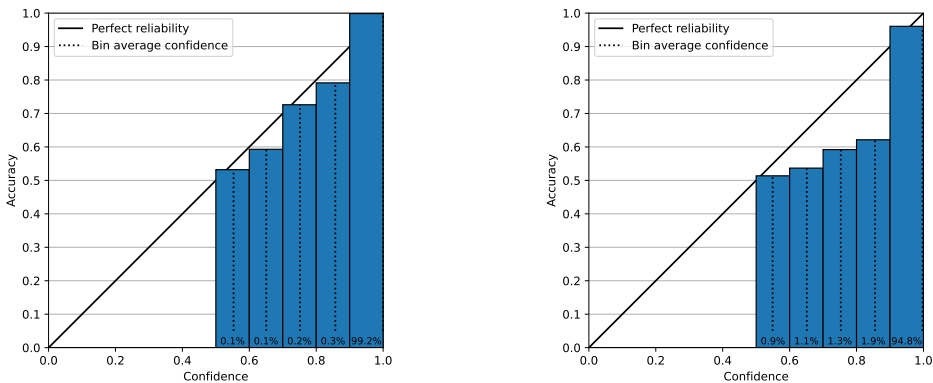


Figure S5. Similar to figure S4 but for the convolutional neural network classifiers used in (left) figure 2b and (right) figure 2c..

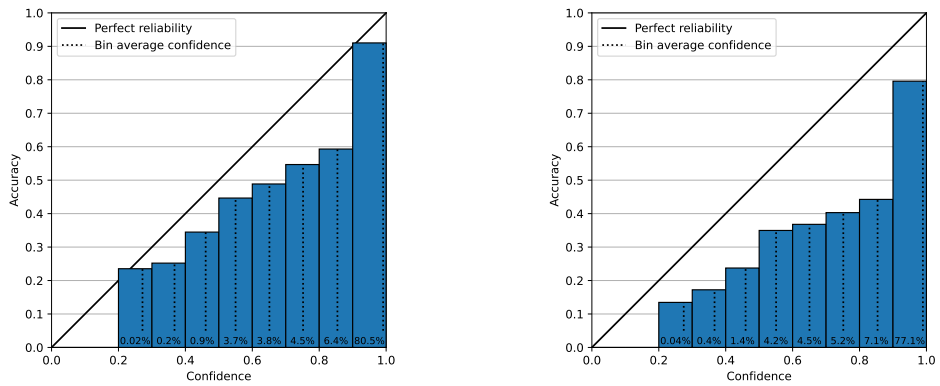


Figure S6. Similar to figure S5 but for the multi-class case shown in (left) figure 3 with test samples from the period 2005-2014 and (right) figure 4 with test samples from the period 2091-2100.

S5. Additional temperature maps

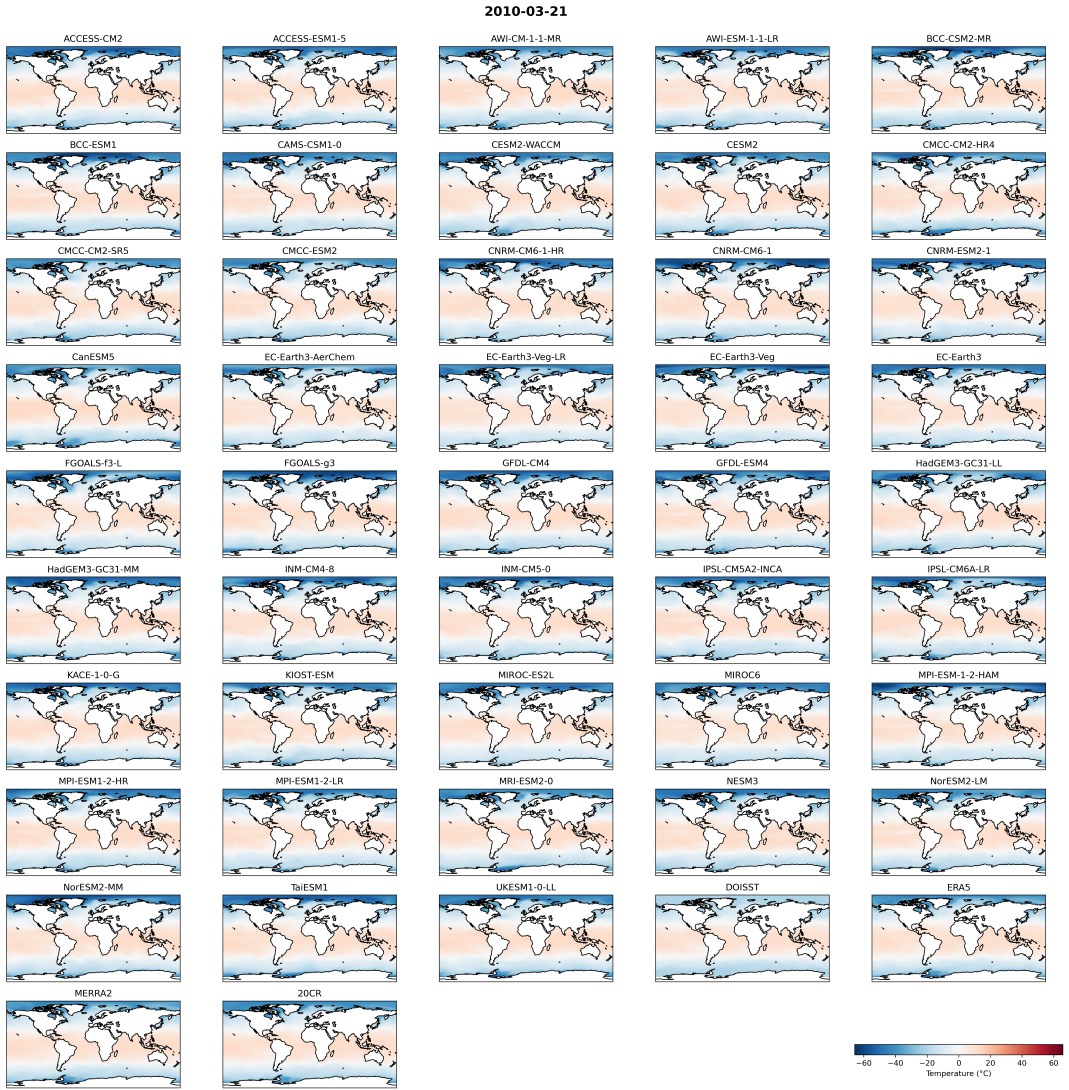


Figure S7. Maps of temperature with the global mean removed for an example day (March 21st 2010) from each of the 43 models and four observational datasets.

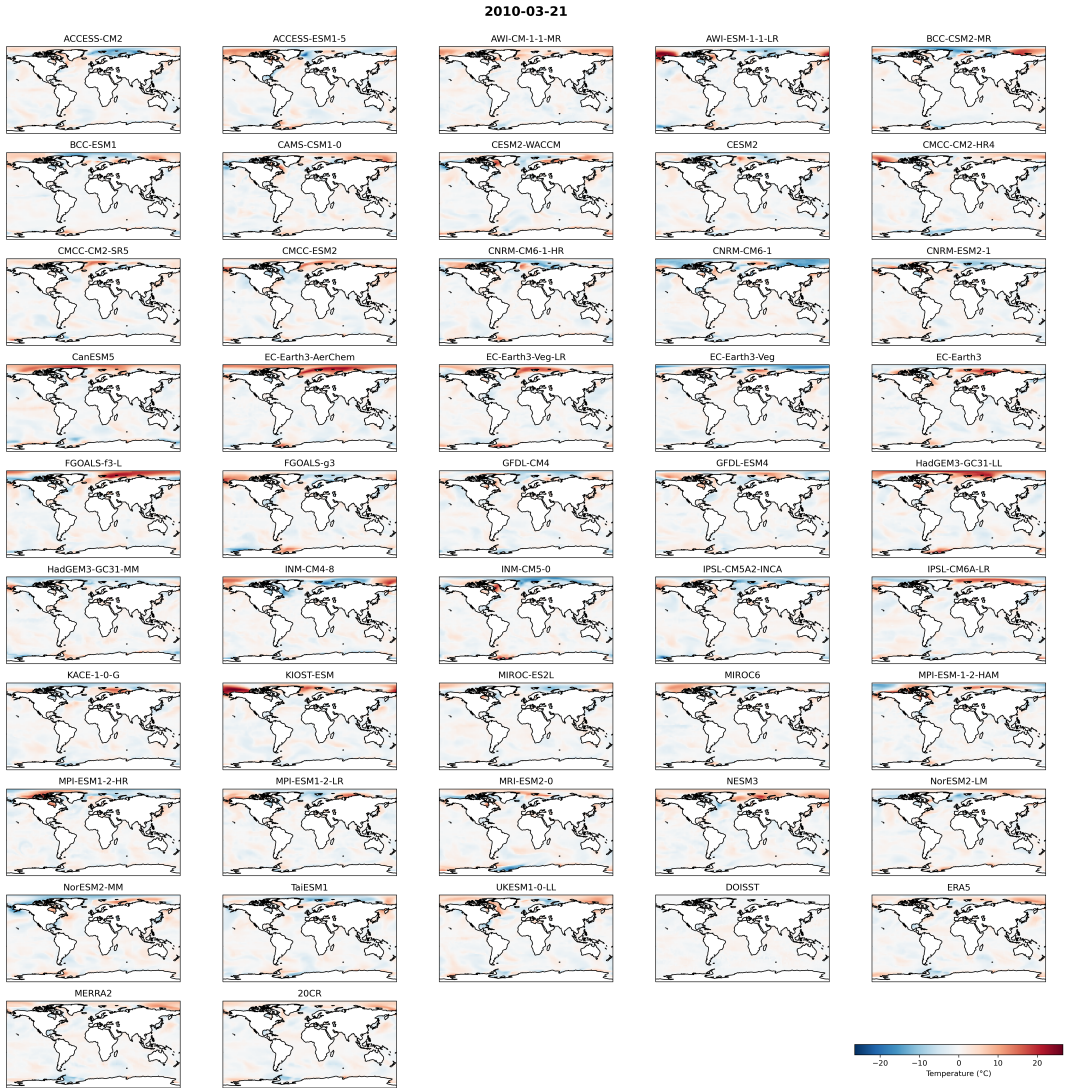


Figure S8. Maps of temperature with the seasonal cycle and the global mean removed for an example day (March 21st 2010) from each of the 43 models and four observational datasets.

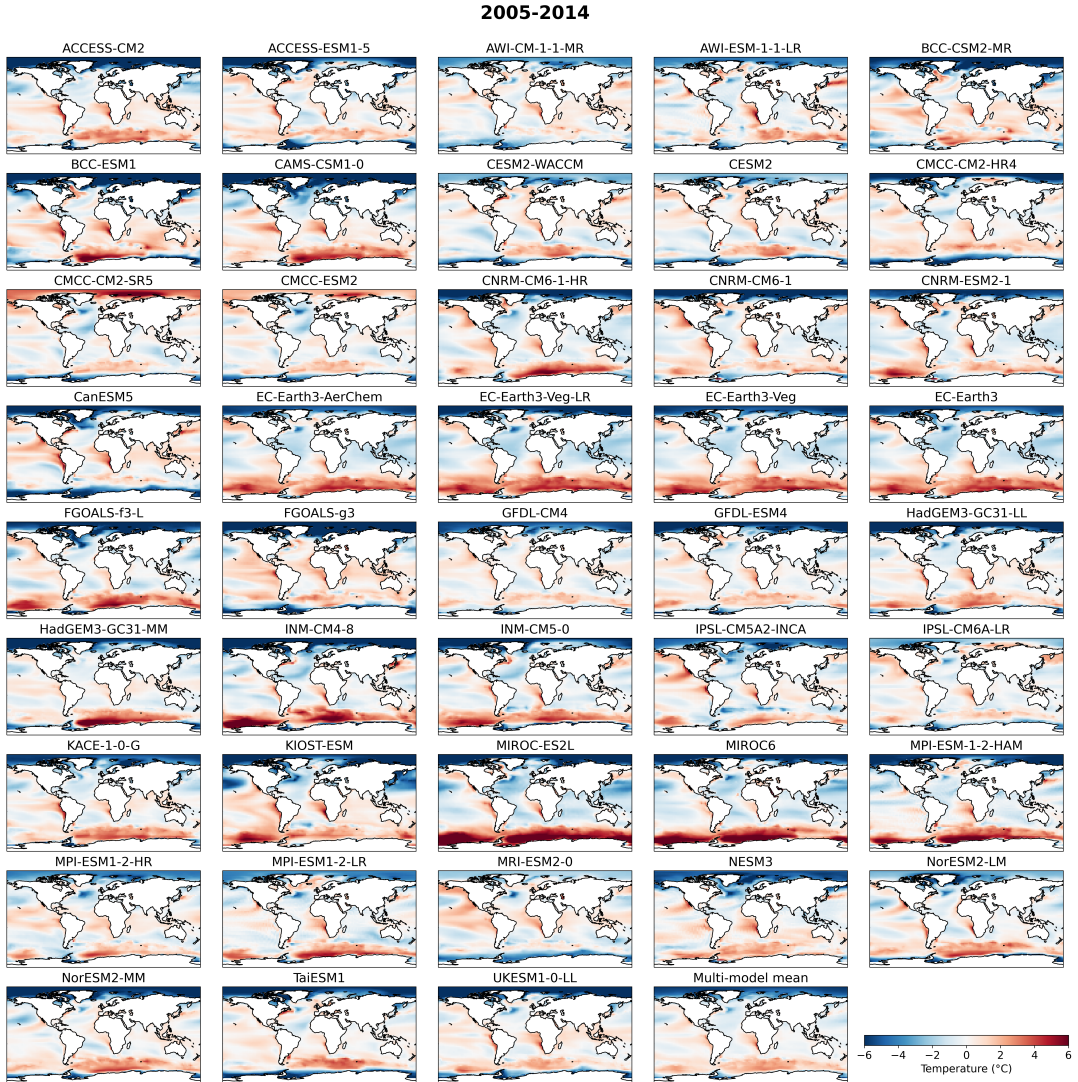


Figure S9. Climatological mean temperature difference from each of the 43 models to the mean over the four observational datasets in the period 2005-2014. The climatologies are calculated from daily data with the global mean removed. The multi-model mean plot in the last panel is identical to figure 1b in the main manuscript and is only shown here for easier comparison.

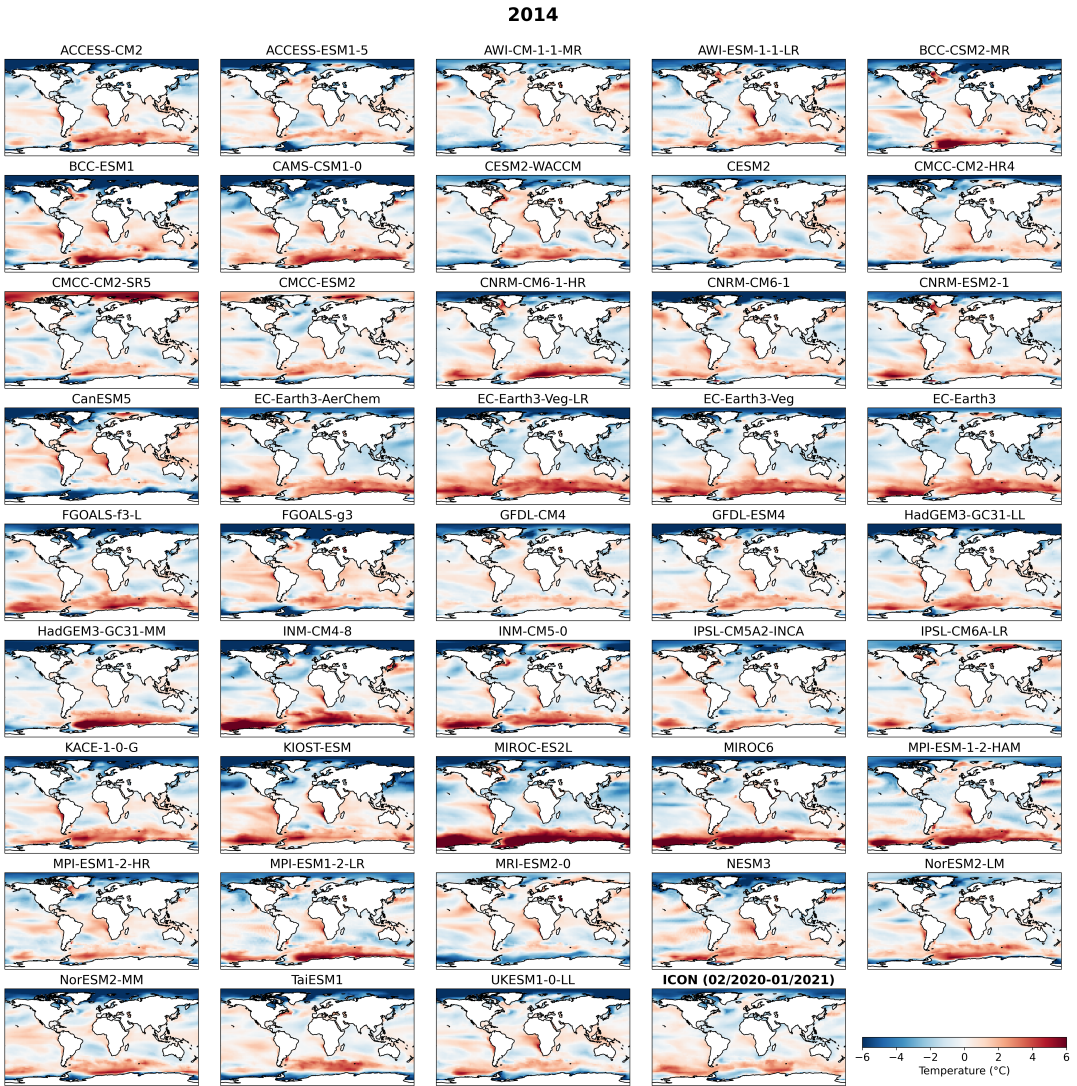


Figure S10. Similar to figure S9 but for only one year (2014) and including differences for ICON in the period February 2020 to January 2021. Note that for the observations the year 2014 is used in all cases.

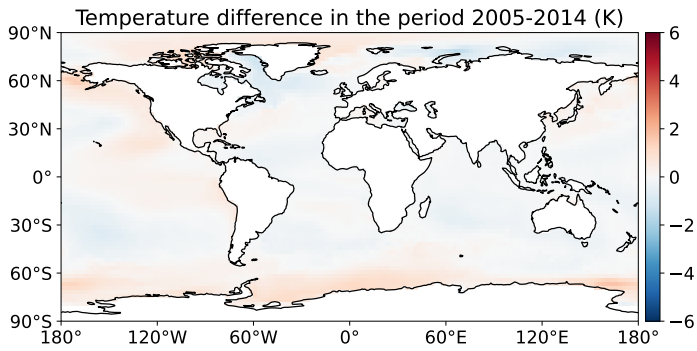


Figure S11. Climatological mean, multi-model mean temperature difference to the mean over the four observational datasets in the period 2005-2014. The climatologies are calculated from daily data with the seasonal cycle and the global mean removed.

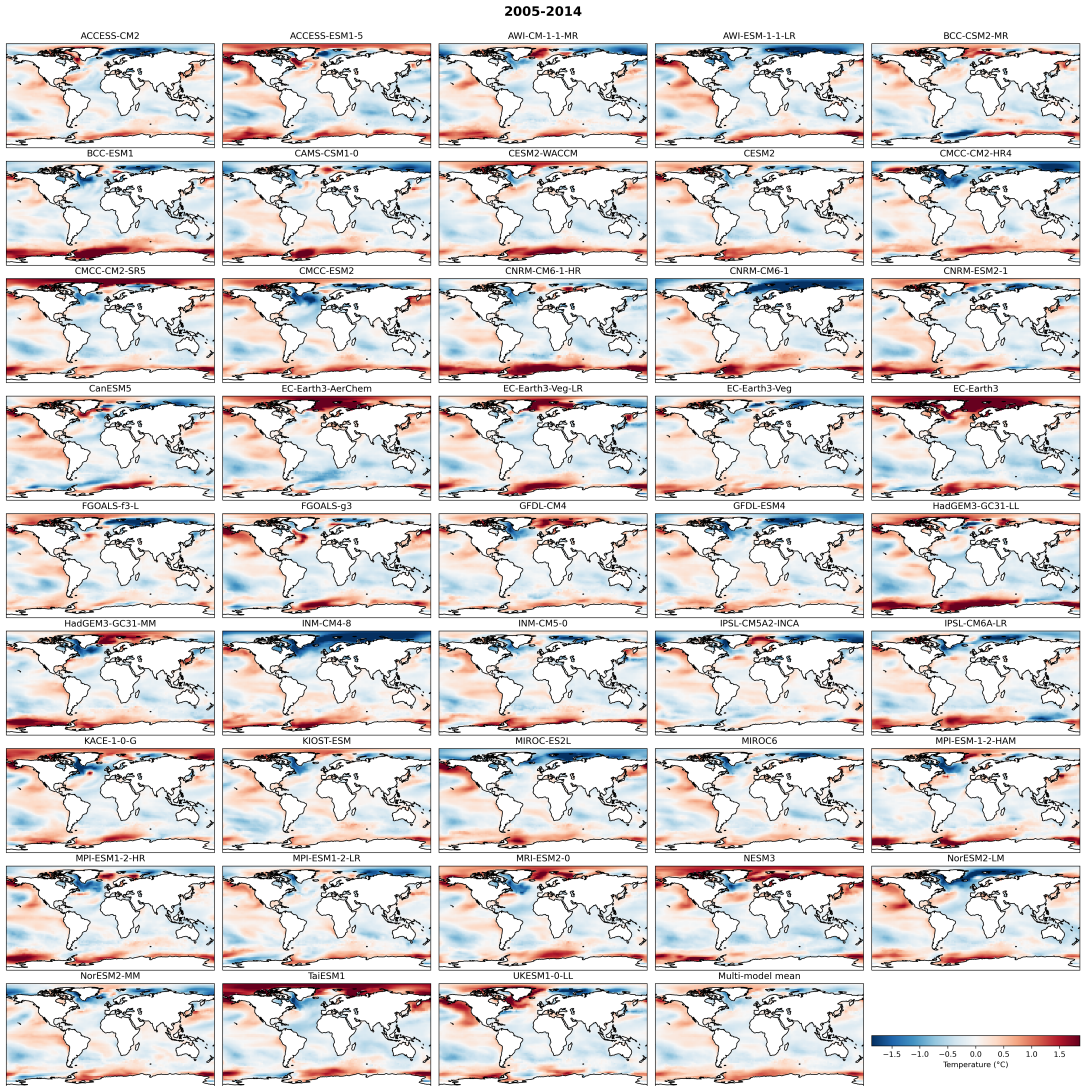


Figure S12. Climatological temperature difference from each of the 43 models to the four observational datasets in the period 2005-2014. The climatologies are calculated from daily data with the seasonal cycle and the global mean removed. The multi-model mean plot (last panel) is similar to figure S11 except for the colormap range and is shown for easier comparison to the individual models.

S6. Models used and model families

Table S3. List of datasets used in this study and related properties.

	Dataset ID	Variant	Family	Type	Future run
1	DOISST	-	observation	observation	no
2	ERA5	-	observation	observation	no
3	MERRA2	-	observation	observation	no
4	20CR	-	observation	observation	no
5	ACCESS-CM2	rlilpf1	ACCESS	model	yes
6	ACCESS-ESM1-5	rlilpf1	ACCESS	model	yes
7	AWI-CM-1-1-MR	rlilpf1	AWI	model	yes
8	AWI-ESM-1-1-LR	rlilpf1	AWI	model	no
9	BCC-CSM2-MR	rlilpf1	BCC	model	yes
10	BCC-ESM1	rlilpf1	BCC	model	no
11	CAMS-CSM1-0	r2ilpf1	CAMS-CSM1-0	model	yes
12	CESM2-WACCM	rlilpf1	CESM	model	no
13	CESM2	rlilpf1	CESM	model	no
14	CMCC-CM2-HR4	rlilpf1	CMCC	model	no
15	CMCC-CM2-SR5	rlilpf1	CMCC	model	yes
16	CMCC-ESM2	rlilpf1	CMCC	model	yes
17	CNRM-CM6-1-HR	rlilpf2	CNRM	model	yes
18	CNRM-CM6-1	rlilpf2	CNRM	model	yes
19	CNRM-ESM2-1	rlilpf2	CNRM	model	yes
20	CanESM5	rlilpf1	CanESM5	model	yes
21	EC-Earth3-AerChem	rlilpf1	EC-Earth	model	no
22	EC-Earth3-Veg-LR	rlilpf1	EC-Earth	model	no
23	EC-Earth3-Veg	rlilpf1	EC-Earth	model	yes
24	EC-Earth3	rlilpf1	EC-Earth	model	yes
25	FGOALS-f3-L	rlilpf1	FGOALS	model	no
26	FGOALS-g3	rlilpf1	FGOALS	model	yes
27	GFDL-CM4	rlilpf1	GFDL	model	yes
28	GFDL-ESM4	rlilpf1	GFDL	model	yes
29	HadGEM3-GC31-LL	rlilpf3	HadGEM	model	yes
30	HadGEM3-GC31-MM	rlilpf3	HadGEM	model	yes
31	INM-CM4-8	rlilpf1	INM	model	yes
32	INM-CM5-0	rlilpf1	INM	model	yes
33	IPSL-CM5A2-INCA	rlilpf1	IPSL	model	no
34	IPSL-CM6A-LR	rlilpf1	IPSL	model	yes
35	KACE-1-0-G	rlilpf1	KACE-1-0-G	model	yes
36	KIOST-ESM	rlilpf1	KIOST-ESM	model	yes
37	MIROC-ES2L	rlilpf2	MIROC	model	yes
38	MIROC6	rlilpf1	MIROC	model	yes
39	MPI-ESM-1-2-HAM	rlilpf1	MPI	model	no
40	MPI-ESM1-2-HR	rlilpf1	MPI	model	yes
41	MPI-ESM1-2-LR	rlilpf1	MPI	model	yes
42	MRI-ESM2-0	rlilpf1	MRI-ESM2-0	model	yes
43	NESM3	rlilpf1	NESM3	model	yes
44	NorESM2-LM	rlilpf1	NorESM2	model	yes
45	NorESM2-MM	rlilpf1	NorESM2	model	yes
46	TaiESM1	rlilpf1	TaiESM1	model	yes
47	UKESM1-0-LL	rlilpf2	HadGEM	model	yes
48	ICON	dpp0066	ICON	model	no

Table S4. List of reference links for the historical datasets used in this study. The numbering corresponds to table S3.

Further information	
1	https://www.ncei.noaa.gov/products/optimum-interpolation-sst
2	https://cds.climate.copernicus.eu/cdsapp#!/dataset/reanalysis-era5-single-levels
3	https://disc.gsfc.nasa.gov/datasets/M2T1NXSLV_5.12.4/summary
4	https://psl.noaa.gov/data/20thC_Rean/
5	https://furtherinfo.es-doc.org/CMIP6.MPI-M.MPI-ESM-1-2-HAM.historical.none.r1i1p1f1
6	https://furtherinfo.es-doc.org/CMIP6.CAMS.CAMS-CSM1-0.historical.none.r2i1p1f1
7	https://furtherinfo.es-doc.org/CMIP6.INM.INM-CM5-0.historical.none.r1i1p1f1
8	https://furtherinfo.es-doc.org/CMIP6.CSIRO-ARCCSS.ACCESS-CM2.historical.none.r1i1p1f1
9	https://furtherinfo.es-doc.org/CMIP6.KIOST.KIOST-ESM.historical.none.r1i1p1f1
10	https://furtherinfo.es-doc.org/CMIP6.CCCma.CanESM5.historical.none.r1i1p1f1
11	https://furtherinfo.es-doc.org/CMIP6.MOHC.UKESM1-0-LL.historical.none.r1i1p1f2
12	https://furtherinfo.es-doc.org/CMIP6.MPI-M.MPI-ESM1-2-HR.historical.none.r1i1p1f1
13	https://furtherinfo.es-doc.org/CMIP6.MOHC.HadGEM3-GC31-MM.historical.none.r1i1p1f3
14	https://furtherinfo.es-doc.org/CMIP6.MRI.MRI-ESM2-0.historical.none.r1i1p1f1
15	https://furtherinfo.es-doc.org/CMIP6.CSIRO.ACCESS-ESM1-5.historical.none.r1i1p1f1
16	https://furtherinfo.es-doc.org/CMIP6.CAS.FGOALS-f3-L.historical.none.r1i1p1f1
17	https://furtherinfo.es-doc.org/CMIP6.NCC.NorESM2-MM.historical.none.r1i1p1f1
18	https://furtherinfo.es-doc.org/CMIP6.EC-Earth-Consortium.EC-Earth3-Veg-LR.historical.none.r1i1p1f1
19	https://furtherinfo.es-doc.org/CMIP6.AWI.AWI-ESM-1-1-LR.historical.none.r1i1p1f1
20	https://furtherinfo.es-doc.org/CMIP6.IPSL.IPSL-CM5A2-INCA.historical.none.r1i1p1f1
21	https://furtherinfo.es-doc.org/CMIP6.AS-RCEC.TaiESM1.historical.none.r1i1p1f1
22	https://furtherinfo.es-doc.org/CMIP6.MIROC.MIROC6.historical.none.r1i1p1f1
23	https://furtherinfo.es-doc.org/CMIP6.IPSL.IPSL-CM6A-LR.historical.none.r1i1p1f1
24	https://furtherinfo.es-doc.org/CMIP6.NOAA-GFDL.GFDL-ESM4.historical.none.r1i1p1f1
25	https://furtherinfo.es-doc.org/CMIP6.EC-Earth-Consortium.EC-Earth3.historical.none.r1i1p1f1
26	https://furtherinfo.es-doc.org/CMIP6.CNRM-CERFACS.CNRM-ESM2-1.historical.none.r1i1p1f2
27	https://furtherinfo.es-doc.org/CMIP6.NIMS-KMA.KACE-1-0-G.historical.none.r1i1p1f1
28	https://furtherinfo.es-doc.org/CMIP6.NCC.NorESM2-LM.historical.none.r1i1p1f1
29	https://furtherinfo.es-doc.org/CMIP6.AWI.AWI-CM-1-1-MR.historical.none.r1i1p1f1
30	https://furtherinfo.es-doc.org/CMIP6.NCAR.CESM2.historical.none.r1i1p1f1
31	https://furtherinfo.es-doc.org/CMIP6.EC-Earth-Consortium.EC-Earth3-AerChem.historical.none.r1i1p1f1
32	https://furtherinfo.es-doc.org/CMIP6.CNRM-CERFACS.CNRM-CM6-1-HR.historical.none.r1i1p1f2
33	https://furtherinfo.es-doc.org/CMIP6.EC-Earth-Consortium.EC-Earth3-Veg.historical.none.r1i1p1f1
34	https://furtherinfo.es-doc.org/CMIP6.BCC.BCC-CSM2-MR.historical.none.r1i1p1f1
35	https://furtherinfo.es-doc.org/CMIP6.NCAR.CESM2-WACCM.historical.none.r1i1p1f1
36	https://furtherinfo.es-doc.org/CMIP6.CAS.FGOALS-g3.historical.none.r1i1p1f1
37	https://furtherinfo.es-doc.org/CMIP6.CMCC.CMCC-CM2-SR5.historical.none.r1i1p1f1
38	https://furtherinfo.es-doc.org/CMIP6.MPI-M.MPI-ESM1-2-LR.historical.none.r1i1p1f1
39	https://furtherinfo.es-doc.org/CMIP6.NUIST.NESM3.historical.none.r1i1p1f1
40	https://furtherinfo.es-doc.org/CMIP6.BCC.BCC-ESM1.historical.none.r1i1p1f1
41	https://furtherinfo.es-doc.org/CMIP6.NOAA-GFDL.GFDL-CM4.historical.none.r1i1p1f1
42	https://furtherinfo.es-doc.org/CMIP6.CMCC.CMCC-ESM2.historical.none.r1i1p1f1
43	https://furtherinfo.es-doc.org/CMIP6.CMCC.CMCC-CM2-HR4.historical.none.r1i1p1f1
44	https://furtherinfo.es-doc.org/CMIP6.INM.INM-CM4-8.historical.none.r1i1p1f1
45	https://furtherinfo.es-doc.org/CMIP6.MIROC.MIROC-ES2L.historical.none.r1i1p1f2
46	https://furtherinfo.es-doc.org/CMIP6.CNRM-CERFACS.CNRM-CM6-1.historical.none.r1i1p1f2
47	https://furtherinfo.es-doc.org/CMIP6.MOHC.HadGEM3-GC31-LL.historical.none.r1i1p1f3
48	https://easy.gems.dkrz.de/DYAMOND/NextGEMS/Models/c1_icon_dpp0066.html

Table S5. List of reference links for the future model runs used in this study. The numbering corresponds to table S3.

	Further information
1	-
2	-
3	-
4	-
5	-
6	https://furtherinfo.es-doc.org/CMIP6.CAMS.CAMS-CSM1-0.ssp585.none.r1i1p1f1
7	https://furtherinfo.es-doc.org/CMIP6.INM.INM-CM5-0.ssp585.none.r1i1p1f1
8	https://furtherinfo.es-doc.org/CMIP6.CSIRO-ARCCSS.ACCESS-CM2.ssp585.none.r1i1p1f1
9	https://furtherinfo.es-doc.org/CMIP6.KIOST.KIOST-ESM.ssp585.none.r1i1p1f1
10	https://furtherinfo.es-doc.org/CMIP6.CCCma.CanESM5.ssp585.none.r1i1p1f1
11	https://furtherinfo.es-doc.org/CMIP6.MOHC.UKESM1-0-LL.ssp585.none.r1i1p1f2
12	https://furtherinfo.es-doc.org/CMIP6.DKRZ.MPI-ESM1-2-HR.ssp585.none.r1i1p1f1
13	https://furtherinfo.es-doc.org/CMIP6.MOHC.HadGEM3-GC31-MM.ssp585.none.r1i1p1f3
14	https://furtherinfo.es-doc.org/CMIP6.MRI.MRI-ESM2-0.ssp585.none.r1i1p1f1
15	https://furtherinfo.es-doc.org/CMIP6.CSIRO.ACCESS-ESM1-5.ssp585.none.r1i1p1f1
16	-
17	https://furtherinfo.es-doc.org/CMIP6.NCC.NorESM2-MM.ssp585.none.r1i1p1f1
18	-
19	-
20	-
21	https://furtherinfo.es-doc.org/CMIP6.AS-RCEC.TaiESM1.ssp585.none.r1i1p1f1
22	https://furtherinfo.es-doc.org/CMIP6.MIROC.MIROC6.ssp585.none.r1i1p1f1
23	https://furtherinfo.es-doc.org/CMIP6.IPSL.IPSL-CM6A-LR.ssp585.none.r1i1p1f1
24	https://furtherinfo.es-doc.org/CMIP6.NOAA-GFDL.GFDL-ESM4.ssp585.none.r1i1p1f1
25	https://furtherinfo.es-doc.org/CMIP6.EC-Earth-Consortium.EC-Earth3.ssp585.none.r1i1p1f1
26	https://furtherinfo.es-doc.org/CMIP6.CNRM-CERFACS.CNRM-ESM2-1.ssp585.none.r1i1p1f2
27	https://furtherinfo.es-doc.org/CMIP6.NIMS-KMA.KACE-1-0-G.ssp585.none.r1i1p1f1
28	https://furtherinfo.es-doc.org/CMIP6.NCC.NorESM2-LM.ssp585.none.r1i1p1f1
29	https://furtherinfo.es-doc.org/CMIP6.AWI.AWI-CM-1-1-MR.ssp585.none.r1i1p1f1
30	-
31	-
32	https://furtherinfo.es-doc.org/CMIP6.CNRM-CERFACS.CNRM-CM6-1-HR.ssp585.none.r1i1p1f2
33	https://furtherinfo.es-doc.org/CMIP6.EC-Earth-Consortium.EC-Earth3-Veg.ssp585.none.r1i1p1f1
34	https://furtherinfo.es-doc.org/CMIP6.BCC.BCC-CSM2-MR.ssp585.none.r1i1p1f1
35	-
36	https://furtherinfo.es-doc.org/CMIP6.CAS.FGOALS-g3.ssp585.none.r1i1p1f1
37	https://furtherinfo.es-doc.org/CMIP6.CMCC.CMCC-CM2-SR5.ssp585.none.r1i1p1f1
38	https://furtherinfo.es-doc.org/CMIP6.MPI-M.MPI-ESM1-2-LR.ssp585.none.r1i1p1f1
39	https://furtherinfo.es-doc.org/CMIP6.NUIST.NESM3.ssp585.none.r1i1p1f1
40	-
41	https://furtherinfo.es-doc.org/CMIP6.NOAA-GFDL.GFDL-CM4.ssp585.none.r1i1p1f1
42	https://furtherinfo.es-doc.org/CMIP6.CMCC.CMCC-ESM2.ssp585.none.r1i1p1f1
43	-
44	https://furtherinfo.es-doc.org/CMIP6.INM.INM-CM4-8.ssp585.none.r1i1p1f1
45	https://furtherinfo.es-doc.org/CMIP6.MIROC.MIROC-ES2L.ssp585.none.r1i1p1f2
46	https://furtherinfo.es-doc.org/CMIP6.CNRM-CERFACS.CNRM-CM6-1.ssp585.none.r1i1p1f2
47	https://furtherinfo.es-doc.org/CMIP6.MOHC.HadGEM3-GC31-LL.ssp585.none.r1i1p1f3
48	